



# Rational design of AgCl@Zr<sup>3+</sup>-ZrO<sub>2</sub> nanostructures for ultra-efficient visible-light photodegradation of emerging pollutants

Xin Yu<sup>a,\*</sup>, Chao Zhou<sup>a</sup>, Zhanhua Huang<sup>b,\*</sup>, Changhui Xin<sup>a</sup>, Yanjing Lin<sup>a</sup>, Fengdan Fu<sup>a</sup>, Shijie Li<sup>c,\*</sup>, Weiping Zhang<sup>d,\*</sup>

<sup>a</sup> Henan Engineering Research Center of Resource & Energy Recovery from Waste, College of Chemistry and Chemical Engineering, Henan University, Kaifeng 475004, China

<sup>b</sup> Key Laboratory of Bio-Based Material Science and Technology, Ministry of Education, College of Material Science and Engineering, Northeast Forestry University, Harbin 150040, China

<sup>c</sup> Key Laboratory of Health Risk Factors for Seafood of Zhejiang Province, Institute of Innovation & Application, Zhejiang Ocean University, Zhoushan, Zhejiang 316022, China

<sup>d</sup> Guangdong Key Laboratory of Environmental Catalysis and Health Risk Control, Guangdong-Hong Kong-Macao Joint Laboratory for Contaminants Exposure and Health, Institute of Environmental Health and Pollution Control, Guangdong University of Technology, Guangzhou 510006, China

## ARTICLE INFO

### Keywords:

Self-doping  
Zirconium dioxide  
Nanostructures  
Emerging contaminants  
Photocatalysis

## ABSTRACT

Achieving high-efficiency charge separation and strong oxidizing capacity are of great significance for photodegradation of organic pollutants. Herein, novel self-doped Zr<sup>3+</sup>-ZrO<sub>2</sub> nanoclusters and AgCl@Zr<sup>3+</sup>-ZrO<sub>2</sub> heterostructures with high surface areas were fabricated for photodegradation of organic pollutants under visible-light illumination. The experimental results revealed that self-doped Zr<sup>3+</sup>-ZrO<sub>2</sub> clusters were formed during a carbothermal reduction process, and the adsorbed surface chlorine promoted the adhesions of Ag<sup>+</sup> to form AgCl over the surface of Zr<sup>3+</sup>-ZrO<sub>2</sub> clusters. The obtained AgCl@Zr<sup>3+</sup>-ZrO<sub>2</sub> heterojunctions displayed ultrahigh-performance degradation of norfloxacin under visible-light illumination, and the prepared AgCl@Zr<sup>3+</sup>-ZrO<sub>2</sub>-11 heterojunction presented the highest photocatalytic performance with a rate constant of 0.21989 min<sup>-1</sup>, which was approximately 62.12 times that of Zr<sup>3+</sup>-ZrO<sub>2</sub> clusters and 21.95 times that of AgCl and far better than that of commercial ZrO<sub>2</sub>. The formation of Zr<sup>3+</sup> self-doping, strongly combined interfaces, and high surface areas highly promoted charge separation for highly enhanced photodegradation of organic pollutants.

## 1. Introduction

Excessive usages and emissions of high-toxic organic substances have caused serious water pollutions and directly affected the survivals of human themselves [1–3]. As a promising strategy to solve serious environmental crisis, photocatalytic technique shows huge advantages in dealing with persistent organic pollutants and gets great concerns [4, 5]. Accordingly, many types of photocatalysts, including single-component and multicomponent photocatalysts, have been prepared for dealing with persistent organic pollutants [6,7]. However, what most troubled us is that some shortcomings, such as the poor redox capacity, narrowed solar-light responsive regions, and poor photocatalytic performance, largely restrict the real applications of semiconductor photocatalysts in dealing with persistent organic pollutants. In addition, some emerging organic pollutants are rather stable and

difficult to be decomposed themselves because of their high oxidation potentials [8,9], such as bisphenol A, norfloxacin, p-hydroxybenzoic acid, and 4-Nitro-m-cresol. And therefore, the fabrications of high-performance and recyclable photocatalysts with strong redox capacity is rather attractive and valuable.

In general, typical ultrawide bandgap semiconductors often have more negative conduction band potentials or more positive valance band potentials compared with traditional narrow bandgap semiconductors, implying huge advantages for generating reactive radicals with strong oxidation capacity. As a typical ultrawide bandgap semiconductor, zirconium dioxide (ZrO<sub>2</sub>) is introduced into the photocatalytic systems for efficiently dealing with persistent organic pollutants in consideration the above obvious advantages [10–12]. However, the biggest difficulty for pristine ZrO<sub>2</sub> is the huge bandgap energy (~5.0 eV), which greatly restricts visible-light harvesting and

\* Corresponding authors.

E-mail addresses: [xinyu@henu.edu.cn](mailto:xinyu@henu.edu.cn) (X. Yu), [huangzh1975@163.com](mailto:huangzh1975@163.com) (Z. Huang), [lishijie@zjou.edu.cn](mailto:lishijie@zjou.edu.cn) (S. Li), [wp.zhang86@gdut.edu.cn](mailto:wp.zhang86@gdut.edu.cn) (W. Zhang).

<https://doi.org/10.1016/j.apcatb.2022.122308>

Received 8 September 2022; Received in revised form 3 December 2022; Accepted 17 December 2022

Available online 20 December 2022

0926-3373/© 2022 Elsevier B.V. All rights reserved.

advanced visible-light photocatalytic applications. Moreover, the relatively severe recombination of photo-generated carriers and fewer active sites also largely affect the surface photocatalytic reactions. Thus, it is still a great challenge and imperative to overcome the above deficiencies to realize high-performance photocatalytic applications of  $\text{ZrO}_2$ . In general, the elemental doping [10,13], fabricating heterostructures [14,15], and self-doping [11,16] are often adopted to modify ultrawide bandgap semiconductors for extended solar-light responsive regions and enhanced charge separation. Nevertheless, the current photocatalytic performances of  $\text{ZrO}_2$ -based photocatalysts still can't meet the needs of large-scale applications and need further improvement. Combining the detailed band structures of  $\text{ZrO}_2$ , recent advances of photocatalytic technique, and urgent requirements for wastewater treatment, novel self-doped  $\text{Zr}^{3+}$ - $\text{ZrO}_2$  clusters with high surface areas are designed and fabricated via a modified solvothermal strategy through carbothermal reduction process for enhanced visible-light harvesting and charge separation under visible-light illumination.

However, pristine self-doped  $\text{Zr}^{3+}$ - $\text{ZrO}_2$  clusters still suffer from obviously poor visible-light harvesting and visible-light photocatalytic performance, and further improved charge separation is urgently needed for efficient removal of emerging organic pollutants [16,17]. Based on this, it is imperative to explore high-performance zirconium-based composite photocatalysts to address the above shortcomings. In recent years, it is reported that integrating hybrid  $\text{Ag}/\text{AgCl}$  or  $\text{AgCl}$  with semiconductors is demonstrated to be a high-efficiency photocatalytic system for highly accelerated charge separation via constructions of heterostructures and localized surface plasmon resonance of  $\text{Ag}^0$  nanoparticles [18,19]. It is worth noting that the prepared  $\text{Zr}^{3+}$ - $\text{ZrO}_2$  clusters have rather high surface areas, implying abundant reactive sites and strong adsorption capacity for organo-inorganic chemical substances. The surface chlorine in  $\text{Zr}^{3+}$ - $\text{ZrO}_2$  nanostructures including  $\text{Cl}^-$  ions would firstly react with  $\text{Ag}^+$  to form  $\text{AgCl}@ \text{Zr}^{3+}$ - $\text{ZrO}_2$  nanostructures, which not only conduce to the harvesting, reflection, and utilization of visible light, but could accelerate charge separation between  $\text{AgCl}$  and  $\text{Zr}^{3+}$ - $\text{ZrO}_2$  clusters. Meanwhile, it could be speculated that abundant  $\text{Ag}$  nanoparticles would be generated over the surface of  $\text{AgCl}$  under visible-light illumination. That is, it is mostly likely that the formed  $\text{Ag}$  nanoparticles are located between  $\text{AgCl}$  and  $\text{Zr}^{3+}$ - $\text{ZrO}_2$  clusters, which would greatly boost the visible-light photocatalytic performances of  $\text{AgCl}@ \text{Zr}^{3+}$ - $\text{ZrO}_2$  heterojunctions under visible-light illumination.

In this work, unique  $\text{Zr}^{3+}$ - $\text{ZrO}_2$  clusters with high surface areas and high-performance  $\text{AgCl}@ \text{Zr}^{3+}$ - $\text{ZrO}_2$  heterojunctions have been fabricated via a modified solvothermal and chemical deposition method. The absorbed surface chlorine over  $\text{Zr}^{3+}$ - $\text{ZrO}_2$  clusters induces the generation of unique  $\text{AgCl}@ \text{Zr}^{3+}$ - $\text{ZrO}_2$  nanostructures. It is also demonstrated that the  $\text{AgCl}@ \text{Zr}^{3+}$ - $\text{ZrO}_2$  heterojunctions exhibit remarkably enhanced photocatalytic performance for photodegradation of organic pollutants under visible-light illumination, including bisphenol A, norfloxacin, 4-Nitro-m-cresol, carbamazepine, and tetracycline, which indicate a strong oxidation capacity and enormous potential of  $\text{AgCl}@ \text{Zr}^{3+}$ - $\text{ZrO}_2$  heterojunctions in dealing with persistent organic pollutants. Accordingly, our work probably provides a high-performance zirconium-based composite photocatalyst for efficiently decomposing organic pollutants under visible-light illumination.

## 2. Experimental section

### 2.1. Chemicals

Commercial Zirconium dioxide ( $\text{ZrO}_2$ , 99.99%), isopropanol ( $\text{C}_3\text{H}_8\text{O}$ , AR, >99.0%), norfloxacin ( $\text{C}_{16}\text{H}_{18}\text{FN}_3\text{O}_3$ , 98%), ethylene glycol ( $\text{C}_2\text{H}_6\text{O}_2$ , AR, 98%), and 4-Nitro-m-cresol (98%, HPLC) were purchased from Shanghai Aladdin Bio-Chem Technology Co., Ltd, China. Zirconyl chloride octahydrate ( $\text{ZrOCl}_2 \cdot 8 \text{H}_2\text{O}$ , 99.9%), methanol ( $\text{CH}_3\text{OH}$ , 99.5%), sodium acetate trihydrate ( $\text{C}_2\text{H}_3\text{O}_2\text{Na} \cdot 3 \text{H}_2\text{O}$ , 99%),

carbamazepine ( $\text{C}_{15}\text{H}_{12}\text{N}_2\text{O}$ , 99%), bisphenol A ( $\text{C}_{15}\text{H}_{16}\text{O}_2$ , >99%), and tetracycline ( $\text{C}_{22}\text{H}_{24}\text{N}_2\text{O}_8$ , CP) were purchased from Macklin Bio-Chemical Technology Co., Ltd, China. Silver nitrate ( $\text{AgNO}_3$ , 99.8%) was purchased from Sinopharm Chemical Reagents Co., Ltd, China. Sodium chloride ( $\text{NaCl}$ , AR) was purchased from Tianjin Chemical One Plant Co., Ltd, China. Acetone ( $\text{CH}_3\text{COCH}_3$ , >99.5%) was purchased from Luoyang Haohua Chemical Reagent Co., Ltd, China. Ethanol ( $\text{CH}_3\text{CH}_2\text{OH}$ , 99.7%) was purchased from Tianjin Fuyu Fine Chemical Co., Ltd, China.

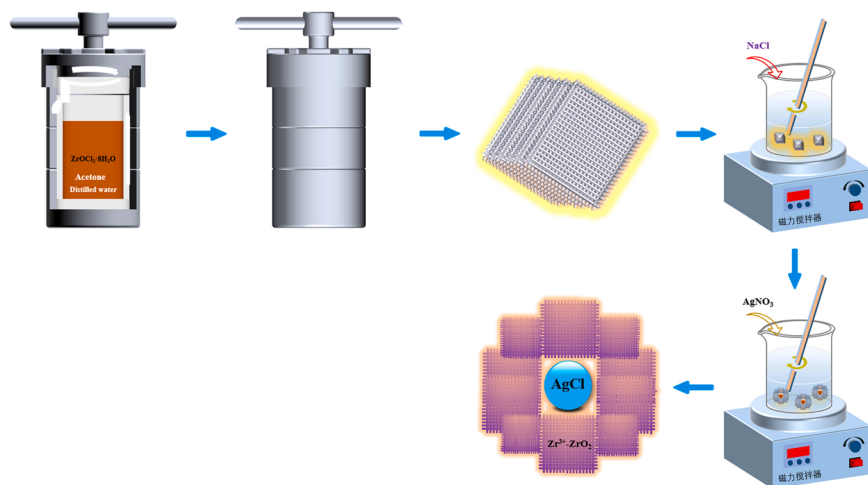
### 2.2. Photocatalyst preparation

Pristine  $\text{Zr}^{3+}$ - $\text{ZrO}_2$  clusters were prepared by a modified solvothermal reaction. In brief, 1.288 g of  $\text{ZrOCl}_2 \cdot 8 \text{H}_2\text{O}$  and 0.164 g of  $\text{C}_2\text{H}_3\text{O}_2\text{Na} \cdot 3 \text{H}_2\text{O}$  were added into a mixture of 5 mL distilled water and 10 mL acetone in a 25 mL Teflon autoclave with stirring for 30 min. Then, the Teflon autoclave was tightened and placed in an oven for reaction at 220 °C for 12 h. After centrifugation, washing with ethanol and distilled water, and drying at 80 °C in an oven for 2 h, the self-doped  $\text{Zr}^{3+}$ - $\text{ZrO}_2$  clusters were obtained.

Hybrid  $\text{AgCl}@ \text{Zr}^{3+}$ - $\text{ZrO}_2$  heterojunctions were firstly prepared by a chemical deposition method. In a typical procedure, 100 mg of  $\text{Zr}^{3+}$ - $\text{ZrO}_2$  clusters were dispersed into 20 mL distilled water with ultrasonication treatment for 5 min. Subsequently, 0.410 mL  $\text{NaCl}$  solution ( $0.10 \text{ g mL}^{-1}$ ) was added into above slurry to form a mixture with stirring. Finally, 2.37 mL  $\text{AgNO}_3$  solution ( $0.05 \text{ g mL}^{-1}$ ) was slowly added into the above mixture with continuous stirring for 30 min. After centrifugation, washing with distilled water and ethanol, and drying at 80 °C in an oven for 2 h, nanostructured  $\text{AgCl}@ \text{Zr}^{3+}$ - $\text{ZrO}_2$  heterojunctions were obtained, and the schematic illustration for the preparation of  $\text{Zr}^{3+}$ - $\text{ZrO}_2$  clusters and  $\text{AgCl}@ \text{Zr}^{3+}$ - $\text{ZrO}_2$  heterojunctions were displayed in Scheme 1. The samples with mass ratios of  $\text{AgCl}$  to  $\text{Zr}^{3+}$ - $\text{ZrO}_2$  of 0.1:1, 0.5:1, 1:1, 2:1, and 3:1 were denoted as the  $\text{AgCl}@ \text{Zr}^{3+}$ - $\text{ZrO}_2$ -0.1,  $\text{AgCl}@ \text{Zr}^{3+}$ - $\text{ZrO}_2$ -0.5,  $\text{AgCl}@ \text{Zr}^{3+}$ - $\text{ZrO}_2$ -1, 2, 3, respectively. In addition, pristine  $\text{AgCl}$  was also prepared as comparison with similar method without adding  $\text{Zr}^{3+}$ - $\text{ZrO}_2$  clusters. In brief, 0.408 g of  $\text{NaCl}$  was dissolved into 40 mL distilled water, and then 1.185 g of  $\text{AgNO}_3$  was slowly added into  $\text{NaCl}$  solution with stirring for 30 min. After centrifugation, washing with ethanol and distilled water, and drying at 80 °C in an oven for 2 h, pristine  $\text{AgCl}$  was obtained.

### 2.3. Characterization

The morphologies were characterized using a JEOL JSM-7610 F scanning electron microscope and an FEI Tecnai G2 F20 transmission electron microscope operating at an acceleration voltage of 200 kV. The crystallized properties and phase structures were identified by using an x-ray diffractometer (Bruker D8 Advance, Germany) with  $\text{Cu K}\alpha$  radiation. Brunauer-Emmett-Teller (BET) surface areas and Barrett-Joiner-Halenda (BJH) pore size distribution curves were obtained on a Quantachrome Autosorb-iQ-MP-C surface area analyzer. The surface chemical states were analyzed by using an ESCALAB 250 Xi electron spectrometer (XPS). Thermal analysis was carried out on a NETZSCH STA 449 F3 analyzer from room temperature to 1200 °C. Optical property was investigated by UV-vis diffuse reflectance spectroscopy on a Shimadzu UV-2600 spectrophotometer. Low temperature EPR spectra were detected by using a Bruker A300-10/12 electron paramagnetic resonance spectrometer with a catalyst dosage of 0.1 g at 77 K. DMPO spin-trapping ESR signals for DMPO-OH and DMPO- $\text{O}_2$  were detected on a Bruker A300 spectrometer (Bruker Corporation). Photoluminescence (PL) spectra were recorded on an Edinburgh FLS980 spectrophotometer with an excitation wavelength of 320 nm. Photoelectrochemical measurements, including electrochemical impedance spectra and Mott-Schottky plots were obtained by using a Chenhua CHI660E electrochemical workstation in 0.1 M  $\text{Na}_2\text{SO}_4$ . The counter electrode, reference electrode, and working electrode were the Pt foil,



**Scheme 1.** Schematic illustration for the preparation of  $\text{Zr}^{3+}\text{-ZrO}_2$  and  $\text{AgCl@Zr}^{3+}\text{-ZrO}_2$  heterojunctions.

saturated calomel electrode, and ITO glass loaded with catalysts, respectively.

#### 2.4. Evaluation of the prepared photocatalysts

A home-made photocatalytic facility equipped with a recirculating cooling water system was used to evaluate the prepared photocatalysts via the degradation of different typical organic pollutants under visible-light illumination. A 400 nm cut-off filter was used to remove the ultraviolet light of a 300 W Xe lamp, and the visible-light intensity is approximately  $578 \text{ mW cm}^{-2}$  obtained by with an optical power meter (CEL-NP2000, CEAULIGHT, Beijing). In a typical procedure, 50 mg of the prepared samples was added into 100 mL norfloxacin solution ( $10 \text{ mg L}^{-1}$ ) to achieve an adsorption-desorption equilibrium in the dark. Then, the photocatalytic system was vertically irradiated by visible light and the degraded norfloxacin solution was taken off from the reactor every 2 min for centrifugation and analysis by a UV-Vis spectrophotometer (Unico UV2150). In addition, some other types of organic pollutants, including bisphenol A, 4-Nitro-m-cresol, carbamazepine, and tetracycline, were also employed as target pollutants to evaluate the prepared  $\text{AgCl@Zr}^{3+}\text{-ZrO}_2$  heterojunctions via a similar method. TOC removal rates of norfloxacin over  $\text{AgCl@Zr}^{3+}\text{-ZrO}_2$  heterojunctions were also analyzed by using an Analytik Jena multiN/C 3100 TOC analyzer.

### 3. Results and discussion

#### 3.1. Morphology, crystallized, and physicochemical property

The detailed morphologies and structures of the as-prepared samples were firstly observed in this work. As shown in Figs. S1(a, b) and Fig. 1(a-d), the prepared  $\text{Zr}^{3+}\text{-ZrO}_2$  sample presents a clusters-like morphology, which is mainly composed of many nanofibers. The average diameter of  $\text{Zr}^{3+}\text{-ZrO}_2$  clusters is approximately  $300 \text{ nm} \times 300 \text{ nm}$  in length and width, and the average diameter of  $\text{Zr}^{3+}\text{-ZrO}_2$  nanofibers is approximately 5 nm. This unique ordered nanostructure often exhibits high surface area and could efficiently utilize visible light through multiple absorbing and reflections, leading to highly improved photocatalytic performance. In addition, the prepared  $\text{Zr}^{3+}\text{-ZrO}_2$  clusters also have high crystallinity, as shown in Fig. 1(c), which is the consequence of oriented adhesions of  $\text{Zr}^{3+}\text{-ZrO}_2$  nanoparticles at a high solvothermal temperature. Fig. 1(e) shows the HRTEM image of  $\text{Zr}^{3+}\text{-ZrO}_2$  clusters, which clearly reveals the detailed morphology of  $\text{Zr}^{3+}\text{-ZrO}_2$  clusters and an interplanar spacing of 0.251 nm, well matching to the (020) crystal plane of  $\text{ZrO}_2$  (JCPDS card No. 01-0750), strongly indicating the formation of  $\text{Zr}^{3+}\text{-ZrO}_2$  phase.

Figs. (f-h) exhibit the morphology of  $\text{AgCl@Zr}^{3+}\text{-ZrO}_2$  heterojunctions with different magnifications. As seen in Fig. 1(f-h), the formed AgCl nanoparticles are encircled by the  $\text{Zr}^{3+}\text{-ZrO}_2$  clusters to form a core-shell nanostructure in a relatively large scale, which is mainly attributed to the bonding effects of surface chlorine with  $\text{Ag}^+$  ions to generate the Ag-Cl chemical bonds. Fig. 1(i) displays the HRTEM image of  $\text{AgCl@Zr}^{3+}\text{-ZrO}_2$  composite, which clearly shows a lattice spacing of 0.233 nm for the (200) crystal plane of AgCl (JCPDS card No. 01-1013) and a lattice spacing of 0.235 nm for the (020) crystal plane of  $\text{Zr}^{3+}\text{-ZrO}_2$  clusters. In view of the above experimental results, it can be demonstrated that the nanostructured  $\text{AgCl@Zr}^{3+}\text{-ZrO}_2$  heterojunctions with combined interfaces have been successfully established.

The phase structures and physicochemical properties were further investigated to well understand the features of the prepared samples. As displayed in Fig. 2(a) and Fig. S2, the major X-ray diffraction peaks for  $\text{Zr}^{3+}\text{-ZrO}_2$  clusters emerging at approximately  $17.37^\circ$ ,  $24.01^\circ$ ,  $27.95^\circ$ ,  $31.36^\circ$ ,  $34.06^\circ$ ,  $50.37^\circ$ , and  $55.30^\circ$  can be assigned to the (100), (110), ( $-111$ ), (111), (020), ( $-221$ ), and (130) crystal planes of  $\text{ZrO}_2$  (JCPDS card No. 01-0750), respectively, much weaker than that of commercial  $\text{ZrO}_2$ . These findings strongly demonstrate the formation of  $\text{Zr}^{3+}\text{-ZrO}_2$  clusters. As shown in Fig. 2(b), the obtained AgCl sample presents three strong X-ray diffraction peaks emerging at  $27.86^\circ$ ,  $32.29^\circ$ ,  $46.28^\circ$ ,  $54.94^\circ$ ,  $57.56^\circ$ ,  $67.31^\circ$ ,  $76.81^\circ$ , and  $85.95^\circ$  without other impurities, which can be readily indexed to the reflections of the (111), (200), (220), (311), (222), (400), (420), and (422) crystal planes of AgCl (JCPDS card No. 01-1013), respectively. As for the prepared  $\text{AgCl@Zr}^{3+}\text{-ZrO}_2$  composites, the XRD patterns are mainly composed of X-ray diffraction signals of AgCl, which confirms the successful introduction of AgCl in the  $\text{Zr}^{3+}\text{-ZrO}_2$  clusters considering TEM results. It is worth noting that no obvious X-ray diffraction signals of  $\text{Zr}^{3+}\text{-ZrO}_2$  clusters are observed for  $\text{AgCl@Zr}^{3+}\text{-ZrO}_2$  heterojunctions, mainly because of the strong crystallinity of AgCl. Apart from this, FT-IR spectroscopy also indicates the successful introduction of AgCl in the  $\text{Zr}^{3+}\text{-ZrO}_2$  nanoclusters, as shown in Fig. 2(c). The absorption band at  $500 \text{ cm}^{-1}$  could be assigned to the characteristic absorption of Zr-O chemical bonds, further indicating the existence of the  $\text{Zr}^{3+}\text{-ZrO}_2$  clusters in the  $\text{AgCl@Zr}^{3+}\text{-ZrO}_2$  heterojunctions [15,20]. In addition, the BET surface areas and BJH pore size distribution of the samples were also studied, as shown in Fig. 2(d), Fig. S3, and Fig. S4. The prepared  $\text{Zr}^{3+}\text{-ZrO}_2$  clusters and  $\text{AgCl@Zr}^{3+}\text{-ZrO}_2$  heterojunction present the type IV isotherms [21,22], indicating the formation of the mesopores in the  $\text{Zr}^{3+}\text{-ZrO}_2$  clusters and  $\text{AgCl@Zr}^{3+}\text{-ZrO}_2$  heterojunctions. The BET surface areas for  $\text{Zr}^{3+}\text{-ZrO}_2$  clusters and  $\text{AgCl@Zr}^{3+}\text{-ZrO}_2$  heterojunction are approximately  $172.758$  and  $62.083 \text{ m}^2 \text{ g}^{-1}$ , respectively, which are much higher than those of AgCl ( $10.088 \text{ m}^2 \text{ g}^{-1}$ ) and



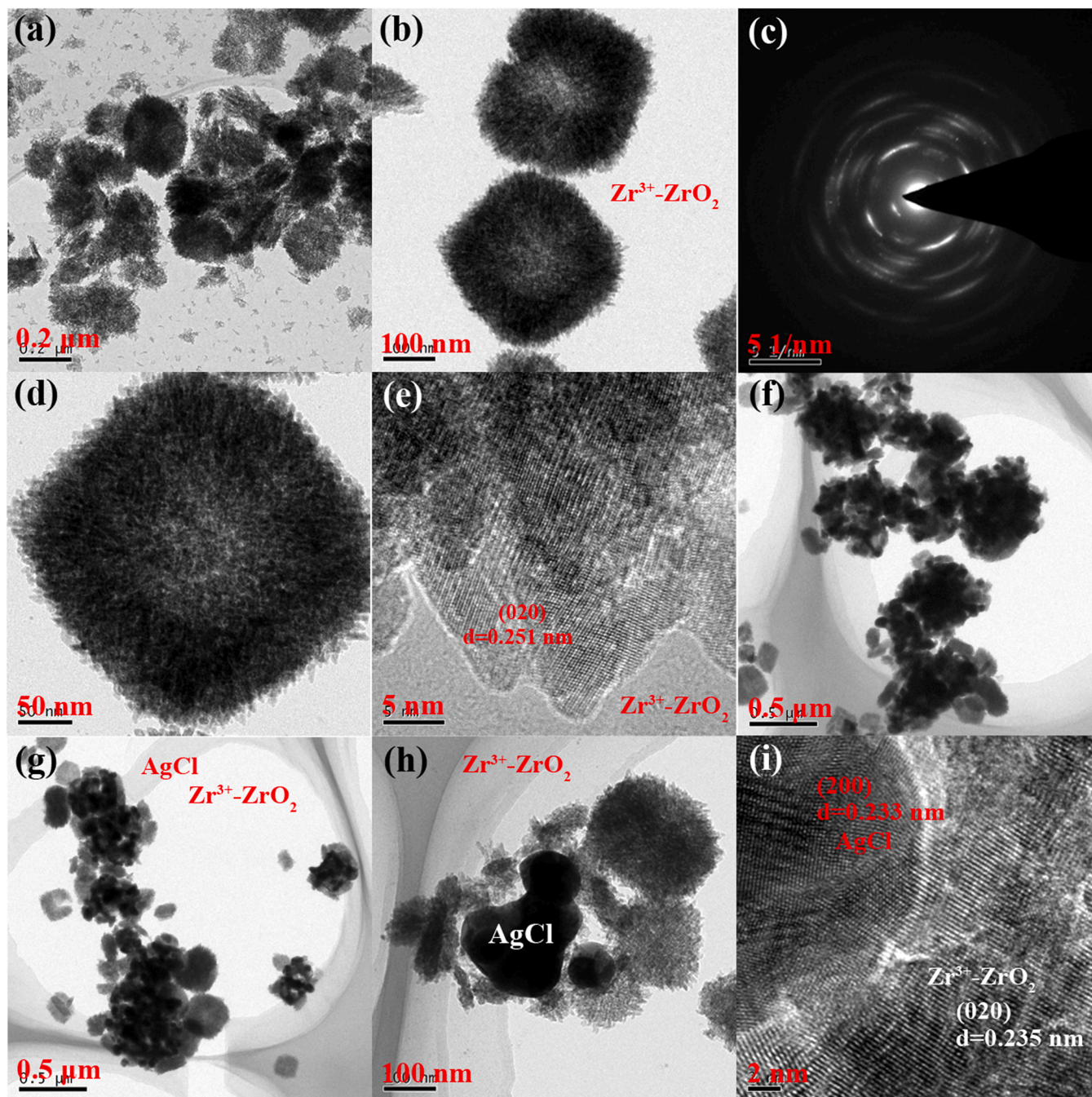


Fig. 1. TEM and HRTEM images for the samples: (a-e)  $\text{Zr}^{3+}\text{-ZrO}_2$ ; (f-i)  $\text{AgCl@Zr}^{3+}\text{-ZrO}_2\text{-11}$  heterojunction.

commercial  $\text{ZrO}_2$  ( $8.992 \text{ m}^2 \text{ g}^{-1}$ ). Very clearly, the BET surface area for  $\text{Zr}^{3+}\text{-ZrO}_2$  clusters is also much higher than those of reported Zr-based semiconductor photocatalysts [9,10,21]. As shown in Fig. S3 and Table 1, the BJH pore-size distribution for  $\text{Zr}^{3+}\text{-ZrO}_2$  clusters and  $\text{AgCl@Zr}^{3+}\text{-ZrO}_2\text{-11}$  heterojunction are mainly located in the mesoporous regions [11,23]. These experimental findings demonstrate the obvious advantages of the  $\text{Zr}^{3+}\text{-ZrO}_2$  clusters and  $\text{AgCl@Zr}^{3+}\text{-ZrO}_2$  heterojunctions in boosting surface photocatalytic reactions.

### 3.2. Composition and elemental analysis

The elemental compositions and chemical states of the samples were analyzed by using X-ray photoelectron spectroscopy. Commercial  $\text{ZrO}_2$  is purchased in this work for comparison. Fig. 3(a) shows the survey XPS

spectra of commercial  $\text{ZrO}_2$ ,  $\text{Zr}^{3+}\text{-ZrO}_2$ , and  $\text{AgCl@Zr}^{3+}\text{-ZrO}_2\text{-11}$  heterojunction. It can be found that the  $\text{AgCl@Zr}^{3+}\text{-ZrO}_2\text{-11}$  heterojunction is mainly composed of C, O, Ag, Zr, and Cl elements. Subsequently, the high-resolution XPS spectroscopy were further tested for well understanding the chemical states of the samples. Fig. 3(b) displays the C 1 s XPS spectrum for the  $\text{AgCl@Zr}^{3+}\text{-ZrO}_2\text{-11}$  heterojunction. The C 1 s XPS spectrum could be fitted in three peaks centered at 284.80, 285.61, and 289.03 eV, corresponding to surface absorbed carbon, carbon of C-OH species, and C=O species, respectively [11,24]. As displayed in Fig. 3 (c), the high-resolution O 1 s XPS spectrum for the  $\text{AgCl@Zr}^{3+}\text{-ZrO}_2\text{-11}$  heterojunction could be fitted into three peaks emerging at 529.95, 531.54, and 532.43 eV, attributing to lattice oxygen atoms, oxygen atoms neighboring to  $\text{Zr}^{3+}$  defects, and surface hydroxide radicals, respectively, which are also close to those of  $\text{Zr}^{3+}\text{-ZrO}_2$  clusters [25,26].



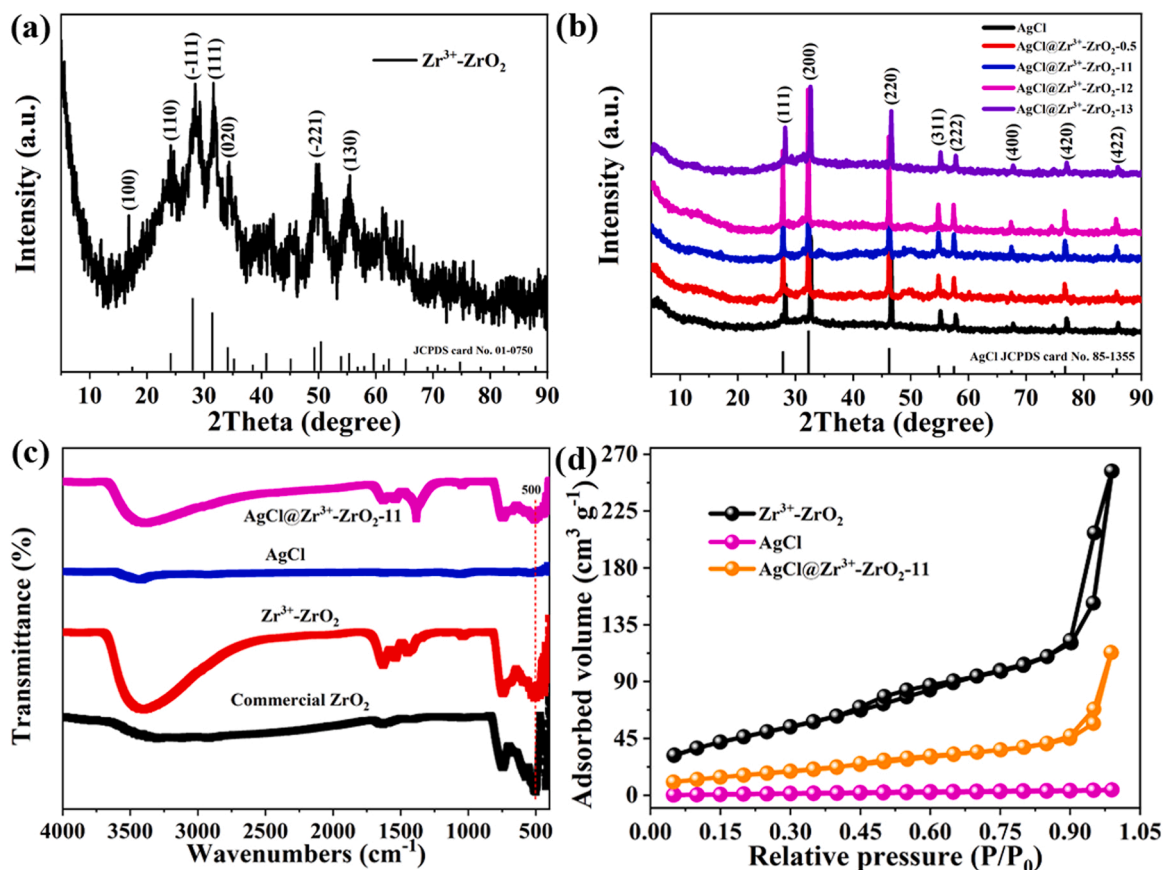


**Fig. 2.** (a) XRD patterns of  $\text{Zr}^{3+}\text{-ZrO}_2$  nanoclusters; (b) XRD patterns of AgCl and AgCl@ $\text{Zr}^{3+}\text{-ZrO}_2$  composites; (c) FT-IR spectra of commercial  $\text{ZrO}_2$ , AgCl,  $\text{Zr}^{3+}\text{-ZrO}_2$ , and AgCl@ $\text{Zr}^{3+}\text{-ZrO}_2$  composites; (d)  $\text{N}_2$  adsorption-desorption isotherms of  $\text{Zr}^{3+}\text{-ZrO}_2$ , AgCl, and AgCl@ $\text{Zr}^{3+}\text{-ZrO}_2$ -11 heterojunction.

**Table 1**

Physico-chemical properties for the  $\text{Zr}^{3+}\text{-ZrO}_2$ , AgCl, and AgCl@ $\text{Zr}^{3+}\text{-ZrO}_2$ -11 heterojunction.

Catalysts	Surface areas ( $\text{m}^2 \text{g}^{-1}$ )	Pore diameter (nm)	Pore volume ( $\text{cm}^3 \text{g}^{-1}$ )
$\text{Zr}^{3+}\text{-ZrO}_2$	172.758	3.402	0.356
AgCl	10.088	3.408	0.006
AgCl@ $\text{Zr}^{3+}\text{-ZrO}_2$ -11	62.083	5.612	0.125

The following high-resolution Zr3d XPS spectra also indicate the generation of  $\text{Zr}^{3+}$  defects in the  $\text{Zr}^{3+}\text{-ZrO}_2$  and AgCl@ $\text{Zr}^{3+}\text{-ZrO}_2$ -11 heterojunction. As depicted in Fig. 3(d), rather obvious shift to higher binding energy compared with that of commercial  $\text{ZrO}_2$  is found with respect to  $\text{Zr}^{3+}\text{-ZrO}_2$  clusters, further indicating the generation of  $\text{Zr}^{3+}$  species [27,28], and similar findings are also observed for the Zr 3d XPS spectrum of AgCl@ $\text{Zr}^{3+}\text{-ZrO}_2$ -11 heterojunction. Note that, the binding energies for Zr 3d XPS spectrum of AgCl@ $\text{Zr}^{3+}\text{-ZrO}_2$ -11 heterojunction are slightly lower than those of  $\text{Zr}^{3+}\text{-ZrO}_2$  but still higher than those of commercial  $\text{ZrO}_2$ , which is mainly attributed to the introduction of AgCl. Fig. 3(e) displays the Cl 2p XPS spectrum in the AgCl and AgCl@ $\text{Zr}^{3+}\text{-ZrO}_2$ -11 heterojunction. Very clearly, the Cl 2p XPS spectrum in the AgCl exhibits two peaks at 198.16 and 199.78 eV, which are well matched with the Cl  $2p_{3/2}$  and Cl  $2p_{1/2}$  of AgCl. However, much different from this, the AgCl@ $\text{Zr}^{3+}\text{-ZrO}_2$ -11 heterojunction displays three fitted peaks located at approximately 195.48, 198.07, and 199.95 eV, respectively. The fitted Cl 2p XPS peaks at 198.07 and 199.95 eV could be assigned to the Cl  $2p_{3/2}$  and Cl  $2p_{1/2}$  of AgCl, but the fitted peak at 195.48 eV could be attributed to surface Cl over the  $\text{Zr}^{3+}\text{-ZrO}_2$  clusters [28,29]. That is to say, the surface Cl elements

perhaps derive from absorbed  $\text{Cl}^-$  ions or the starting material of  $\text{ZrOCl}_2 \cdot 8\text{H}_2\text{O}$ , which plays crucial roles in forming unique AgCl@ $\text{Zr}^{3+}\text{-ZrO}_2$  nanostructure. Fig. 3(f) shows the Ag MN1 X-ray excited auger electron spectroscopy (XAES) spectroscopy for the fresh and used AgCl@ $\text{Zr}^{3+}\text{-ZrO}_2$ -11 heterojunction. It can be seen the AgCl@ $\text{Zr}^{3+}\text{-ZrO}_2$ -11 heterojunction shows no signals of  $\text{Ag}^0$ , also agreeing well with the XRD characterization, while obvious  $\text{Ag}^0$  and  $\text{Ag}^+$  (Ag-Cl) signals can be found for the used AgCl@ $\text{Zr}^{3+}\text{-ZrO}_2$ -11 heterojunction. The atomic percentages of  $\text{Ag}^0$  and  $\text{Ag}^+$  (Ag-Cl) for the used AgCl@ $\text{Zr}^{3+}\text{-ZrO}_2$ -11 heterojunction are 27.07% and 72.93%, respectively.

### 3.3. Visible-light photocatalytic performance

Visible-light photocatalytic performance and recyclable stability were investigated via the degradation of target organic pollutants in a home-made facility. The intensity of visible-light illumination in this part is approximately  $578 \text{ mW cm}^{-2}$ , and the dosage of the catalysts is 50 mg. As displayed in Fig. 4(a), commercial  $\text{ZrO}_2$  exhibits no photocatalytic performance towards norfloxacin degradation under visible-light irradiation as expected mainly owing to its ultrawide bandgap energy of approximately 5.0 eV. However, the prepared AgCl and  $\text{Zr}^{3+}\text{-ZrO}_2$  clusters exhibit relatively poor photocatalytic performance under visible-light illumination. To our surprise, the prepared AgCl@ $\text{Zr}^{3+}\text{-ZrO}_2$  heterojunctions exhibit remarkably improved visible-light photocatalytic performance, and the prepared AgCl@ $\text{Zr}^{3+}\text{-ZrO}_2$ -11 heterojunction presents the highest photocatalytic performance compared with those of commercial  $\text{ZrO}_2$ , AgCl, and  $\text{Zr}^{3+}\text{-ZrO}_2$  clusters. The rate constants of the samples were obtained by the fitted first-order-kinetic plots and exhibited in Fig. 4(b). The apparent rate constants for the  $\text{Zr}^{3+}\text{-ZrO}_2$ , AgCl, and AgCl@ $\text{Zr}^{3+}\text{-ZrO}_2$ -11 heterojunction towards

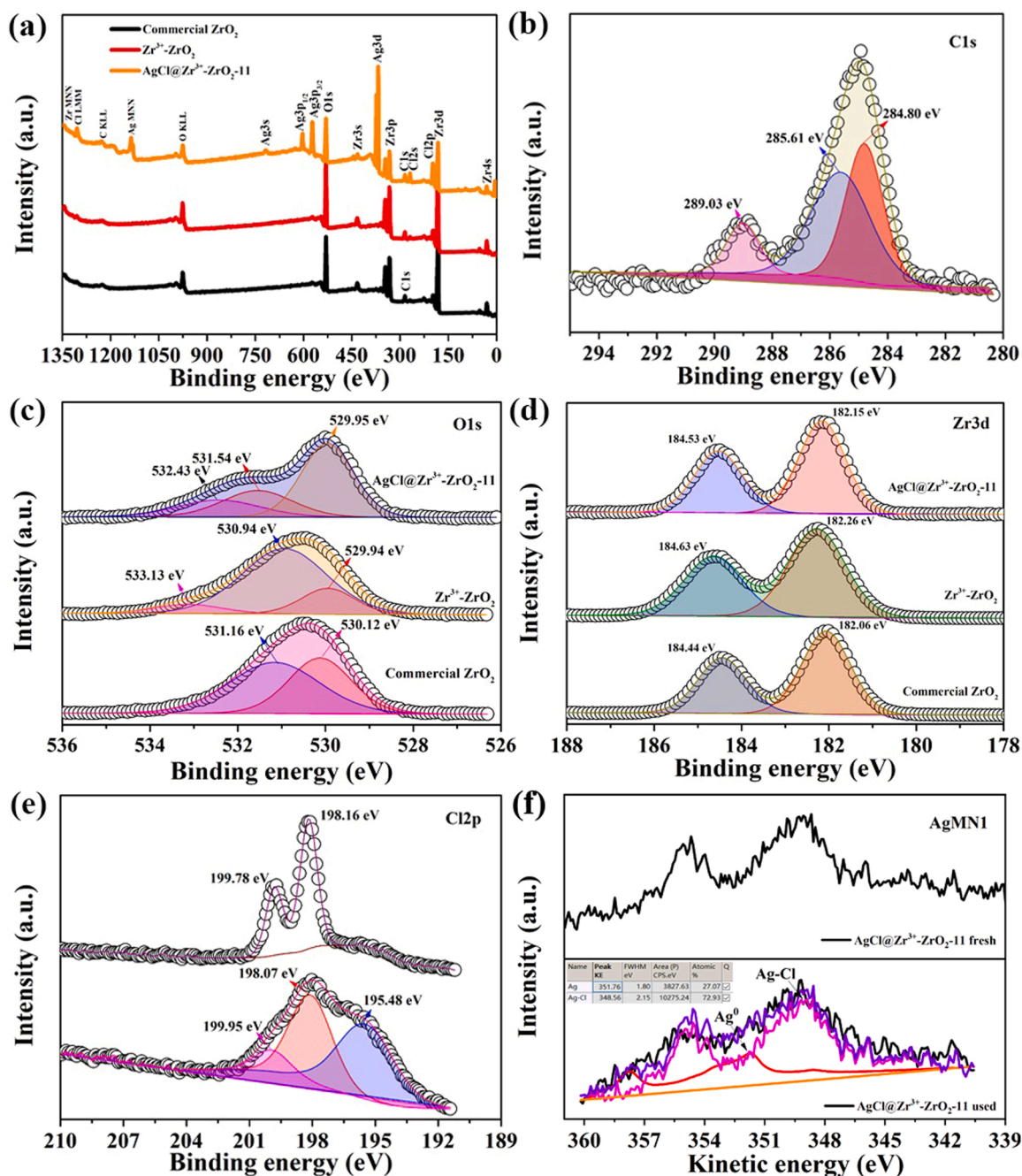
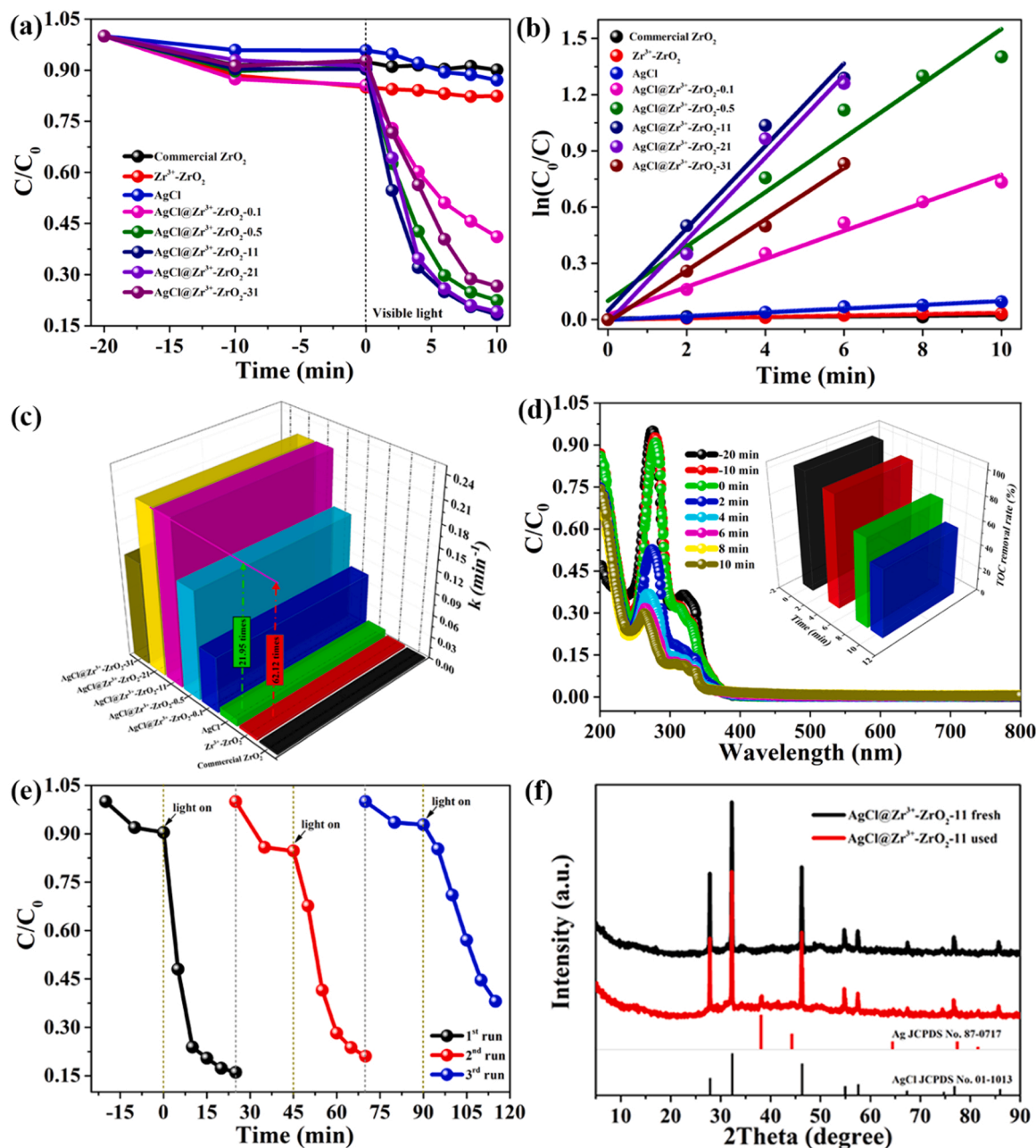


Fig. 3. XPS and XAES spectra for the samples: (a) Survey; (b) C 1 s; (c) O 1 s; (d) Ag 3d; (e) Cl 2p; (f) Ag MN1.

norfloxacin degradation are calculated to be approximately 0.00354, 0.01002, and 0.21989 min<sup>-1</sup>, respectively. To directly observe the outstanding photocatalytic performance of AgCl@Zr<sup>3+</sup>-ZrO<sub>2</sub> heterojunctions, the apparent rate constants are displayed in Fig. 4(c), revealing that the apparent rate constant for the AgCl@Zr<sup>3+</sup>-ZrO<sub>2</sub>-11 heterojunction is approximately 62.12 times that of Zr<sup>3+</sup>-ZrO<sub>2</sub> and 21.95 times that of AgCl, far better than commercial ZrO<sub>2</sub>. The insert in Fig. 4(d) shows TOC removal rates by the AgCl@Zr<sup>3+</sup>-ZrO<sub>2</sub>-11 heterojunction at different visible-light illumination times, which reveals a rapidly increased TOC removal rates for the prepared AgCl@Zr<sup>3+</sup>-ZrO<sub>2</sub>-11 heterojunction. Fig. 4(d) shows the time-dependent UV-Vis absorption changes of the degraded norfloxacin solution. We could easily observe an obvious adsorption-desorption equilibrium in the dark and a sharply decreased UV-vis absorbance at 272 nm, also indicating the remarkably enhanced photocatalytic degradation performance of AgCl@Zr<sup>3+</sup>-ZrO<sub>2</sub>

heterojunctions. Fig. 4(e) shows the visible-light photocatalytic performance of AgCl@Zr<sup>3+</sup>-ZrO<sub>2</sub>-11 heterojunction through three cycles. It can be easily found that the prepared AgCl@Zr<sup>3+</sup>-ZrO<sub>2</sub>-11 heterojunction shows a relatively good stability towards norfloxacin degradation. In addition, the X-ray diffraction patterns of AgCl@Zr<sup>3+</sup>-ZrO<sub>2</sub>-11 heterojunction after photocatalytic reaction were also studied, as depicted in Fig. 4(f). It can be found that obvious Ag<sup>0</sup> is generated from the decomposition of AgCl after visible-light illumination. That is, the generation of Ag<sup>0</sup> take place under visible-light irradiation, and there is no formation of Ag<sup>0</sup> for pristine AgCl@Zr<sup>3+</sup>-ZrO<sub>2</sub> heterojunctions, which is also consistent with the above XRD and XAES characterizations. Apart from this, some critical experimental parameters, such as the dosages of the catalyst, norfloxacin concentrations, visible light intensities, and initial pH values, were also studied in detail. As shown in Fig. S5(a), we could find that the photocatalytic performance increases with an



**Fig. 4.** (a, b) Photocatalytic norfloxacin degradation curves under visible-light illumination and the first-order-kinetic plots; (c) Comparison of the apparent rate constants; (d) Time-dependent UV-vis absorption of the degraded norfloxacin solution at irradiation times (insert indicates the TOC removal rate enabled by AgCl@Zr<sup>3+</sup>-ZrO<sub>2</sub>-11 heterojunction under visible-light illumination); (e) Recyclable photocatalytic performance for the AgCl@Zr<sup>3+</sup>-ZrO<sub>2</sub>-11 heterojunction under visible-light illumination; (f) Comparison of XRD patterns of the fresh and used AgCl@Zr<sup>3+</sup>-ZrO<sub>2</sub>-11 heterojunctions.

increase of catalyst dosage from 25 mg to 75 mg for AgCl@Zr<sup>3+</sup>-ZrO<sub>2</sub>-11 heterojunction, and the photocatalytic performance nearly remains the same though the catalyst dosage increases to 100 mg, indicating that the optimal catalyst dosage is approximately 75 mg in this work. Fig. S5(b) shows the effects of norfloxacin concentrations on the photocatalytic performance of AgCl@Zr<sup>3+</sup>-ZrO<sub>2</sub>-11 heterojunction. It can be found that high norfloxacin concentrations are not conducive to photocatalytic performance, and two close degradation curves are found when the norfloxacin concentration increases from 5 mg L<sup>-1</sup> to 10 mg L<sup>-1</sup>, indicating that the desired norfloxacin concentration is perhaps 10 mg L<sup>-1</sup>. The following measurements indicate that visible-light harvesting is not a dominant parameter for the AgCl@Zr<sup>3+</sup>-ZrO<sub>2</sub>-11 heterojunction in this work, as shown in Fig. S5(c). Finally, the influences of pH values on photocatalytic performance of the AgCl@Zr<sup>3+</sup>-ZrO<sub>2</sub>-11 heterojunction

were also studied, as displayed in Fig. S5(d). It is found that the neutral environment is perhaps more suitable for norfloxacin degradation compared with alkaline and acid environments over AgCl@Zr<sup>3+</sup>-ZrO<sub>2</sub> composites.

To highlight the wide applications and strong oxidation capacity of the prepared AgCl@Zr<sup>3+</sup>-ZrO<sub>2</sub> heterojunctions, some other typical organic pollutants, including bisphenol A, 4-Nitro-m-cresol, carbamazepine, and tetracycline, were chosen as the target pollutants to fully evaluate the prepared AgCl@Zr<sup>3+</sup>-ZrO<sub>2</sub> heterojunctions. As presented in Fig. 5(a-c), commercial ZrO<sub>2</sub>, AgCl, and Zr<sup>3+</sup>-ZrO<sub>2</sub> clusters shows no obvious visible-light photocatalytic performance towards bisphenol A degradation, while a remarkably enhanced photocatalytic performance is observed for the AgCl@Zr<sup>3+</sup>-ZrO<sub>2</sub>-11 heterojunction. The apparent rate constant is as high as 0.052 min<sup>-1</sup>, far superior to those of



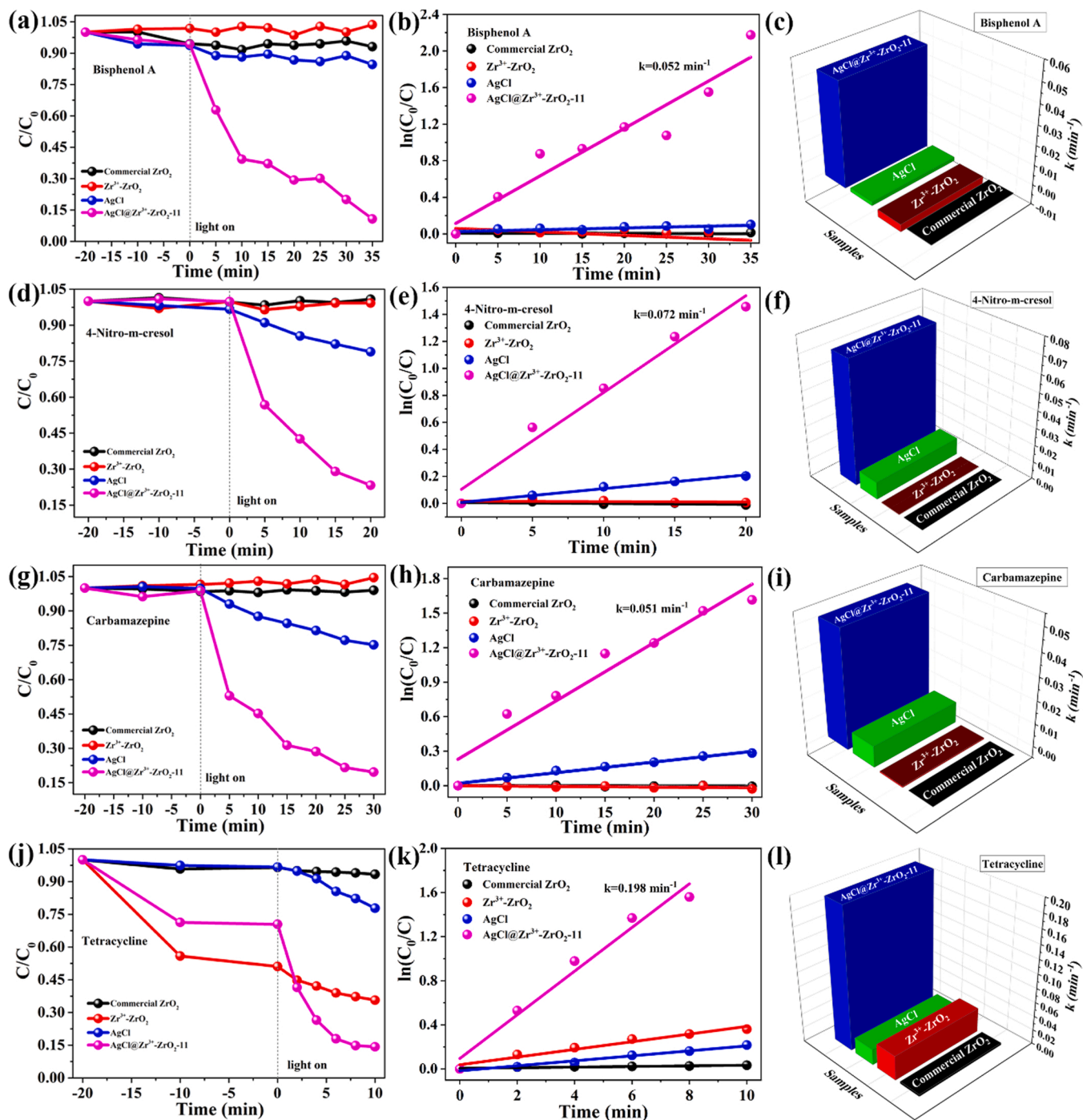


**Fig. 5.** Visible-light photocatalytic performances of the samples for dealing with different organic pollutants, the corresponding first-order-kinetic plots, and comparisons of the apparent rate constants: (a-c) Bisphenol A; (d-f) 4-Nitro-m-cresol; (g-i) Carbamazepine; (j-l) Tetracycline.

commercial  $ZrO_2$ , AgCl, and  $Zr^{3+}$ - $ZrO_2$ . It should be also pointed out that the photocatalytic degradation efficiency of bisphenol A could reach nearly 100% in 35 min. Likewise, the prepared AgCl@ $Zr^{3+}$ - $ZrO_2$ -11 heterojunction is also employed to deal with the 4-Nitro-m-cresol, as displayed in Fig. 5(d-f). The prepared AgCl@ $Zr^{3+}$ - $ZrO_2$ -11 heterojunction also shows an exceptionally enhanced photocatalytic performance compared with those of commercial  $ZrO_2$ , AgCl, and  $Zr^{3+}$ - $ZrO_2$  clusters, and the corresponding rate constant reaches as high as  $0.072 \text{ min}^{-1}$ . Fig. 5(g-i) present the photocatalytic degradation curves of the AgCl@ $Zr^{3+}$ - $ZrO_2$ -11 heterojunction for carbamazepine degradation. A remarkably enhanced photocatalytic performance is observed for AgCl@ $Zr^{3+}$ - $ZrO_2$ -11 heterojunction compared with those of commercial

$ZrO_2$ ,  $Zr^{3+}$ - $ZrO_2$ , and AgCl. The apparent rate constant reaches as high as  $0.051 \text{ min}^{-1}$  for AgCl@ $Zr^{3+}$ - $ZrO_2$ -11 heterojunction, showing tremendous potential for heterocycle compound degradation. Finally, the AgCl@ $Zr^{3+}$ - $ZrO_2$ -11 heterojunction also exhibits ultrahigh-performance photodegradation of tetracycline under visible-light illumination, still far better than those of commercial  $ZrO_2$ ,  $Zr^{3+}$ - $ZrO_2$ , and AgCl, as displayed in Fig. 5(j-l). In a word, the prepared AgCl@ $Zr^{3+}$ - $ZrO_2$  heterojunctions could efficiently deal with many types of organic pollutants under visible-light illumination, seeming much better than those of reported AgCl/MIL-100(Fe) [30], Ag/AgCl/ $Ta_2O_5-x$  [31], Ag/AgCl/BiOCl [32], AgCl/Ag/ $In_2O_3$  [33], and Ag/AgCl/ $In_2O_3$  [34], also indicating obvious advantages of nanostructured AgCl@ $Zr^{3+}$ - $ZrO_2$  heterojunctions

for high-performance environmental photocatalysis.

### 3.4. Visible-light photocatalytic mechanism

To well understand the main reactive radicals in the visible-light photocatalytic norfloxacin degradation over nanostructured  $\text{AgCl@Zr}^{3+}\text{-ZrO}_2$  heterojunctions under visible-light illumination, trapping experiments of active species were carried out by adding different scavengers, including methanol,  $\text{N}_2$ , and isopropanol [11,31]. In this work, methanol (1 mM) is used as the  $\text{h}^+$  scavengers, and  $\text{N}_2$  and isopropanol (1 mM) are employed as the  $\bullet\text{O}_2^-$  and  $\bullet\text{OH}$  radical scavengers, respectively [11,35]. As shown in Fig. 6(a, b), the addition of methanol induces a decreased photocatalytic performance for the  $\text{AgCl@Zr}^{3+}\text{-ZrO}_2$ -11 heterojunction, while the additions of  $\text{N}_2$  and isopropanol also cause the decreases of the photocatalytic performances, which indicate that the photo-generated holes,  $\bullet\text{O}_2^-$  and  $\bullet\text{OH}$  radicals play crucial roles in norfloxacin degradation under visible-light illumination [36,37]. Besides, ESR spectra trapped by 5,5-dimethyl-1-pyrroline-N-oxide (DMPO) was further measured to verify the types of the reactive radicals over the  $\text{AgCl@Zr}^{3+}\text{-ZrO}_2$  heterojunctions, as shown in Fig. 6(c, d). It can be found that obvious DMPO- $\bullet\text{O}_2^-$  and DMPO- $\bullet\text{OH}$  signals can be detected under visible-light illumination but no ESR signals are observed in the dark. These findings confirm that  $\bullet\text{O}_2^-$  and  $\bullet\text{OH}$  species are also generated under visible-light illumination over  $\text{AgCl@Zr}^{3+}\text{-ZrO}_2$  heterojunctions [38,39]. In addition, the surface chemical states of the used  $\text{AgCl@Zr}^{3+}\text{-ZrO}_2$ -11 heterojunction after visible-light irradiation compared with those of fresh  $\text{AgCl@Zr}^{3+}\text{-ZrO}_2$  heterojunctions were also studied by X-ray photoelectron spectroscopy and UV-vis diffuse reflection absorption spectroscopy. As shown in Fig. S6(a), the used  $\text{AgCl@Zr}^{3+}\text{-ZrO}_2$ -11 heterojunction exhibits similar chemical compositions as those of the fresh  $\text{AgCl@Zr}^{3+}\text{-ZrO}_2$ -11

heterojunction. Fig. S6(b) shows the UV-vis diffuse reflection absorption spectroscopy of the fresh and used  $\text{AgCl@Zr}^{3+}\text{-ZrO}_2$ -11 heterojunctions. It is clearly revealed that the used  $\text{AgCl@Zr}^{3+}\text{-ZrO}_2$ -11 heterojunction presents remarkably enhanced visible-light absorption compared with that of fresh  $\text{AgCl@Zr}^{3+}\text{-ZrO}_2$ -11 heterojunction, mainly because of the formation of  $\text{Ag}^0$  after visible-light irradiation [40,41]. These findings are also consistent with results of XRD patterns of the fresh and used  $\text{AgCl@Zr}^{3+}\text{-ZrO}_2$ -11 heterojunctions in Fig. 4(f). That is, a small amount of  $\text{AgCl}$  decomposes to  $\text{Ag}^0$  and highly improves visible-light harvesting and charge separation.

We also investigated the optical property, energy band structures, and the formation of  $\text{Zr}^{3+}$  species. As shown in Fig. 7(a), the obtained  $\text{Zr}^{3+}\text{-ZrO}_2$  clusters exhibit obvious visible-light absorption compared with that of commercial  $\text{ZrO}_2$ , mainly because of the formation of  $\text{Zr}^{3+}$  species. It is also found that the prepared  $\text{AgCl@Zr}^{3+}\text{-ZrO}_2$  heterojunctions exhibit an improved solar-light absorption before 400 nm, which is mainly attributed to the introduction of  $\text{AgCl}$  but still lower than that of  $\text{AgCl}$ . Note that no enhanced visible-light absorption is observed for the  $\text{AgCl}$  and  $\text{AgCl@Zr}^{3+}\text{-ZrO}_2$ -11 heterojunction. These results also indicate that there is no generation of  $\text{Ag}^0$  for the  $\text{AgCl}$  and  $\text{AgCl@Zr}^{3+}\text{-ZrO}_2$ -11 heterojunction, also demonstrating the formation  $\text{AgCl@Zr}^{3+}\text{-ZrO}_2$  heterojunctions. The detailed bandgap energies were evaluated according to Kubelka-Munk equation, as shown in Fig. 7(b). The bandgap energies for the prepared  $\text{AgCl}$  and  $\text{Zr}^{3+}\text{-ZrO}_2$  clusters are calculated to be approximately 3.07 and 5.13 eV, respectively [42]. In addition, possible reasons for enhanced visible-light absorption and the formation of  $\text{Zr}^{3+}$  species were also investigated in detail. As shown in Fig. 7(c), the low temperature electron paramagnetic resonance (EPR) spectrum for  $\text{Zr}^{3+}\text{-ZrO}_2$  clusters at 77 K exhibits two strong signals at  $g = 1.93$  and 2.00, which could be ascribed to the surface  $\text{Zr}^{3+}$  species and single-electron-trapped oxygen vacancies [11,12,43,44], strongly

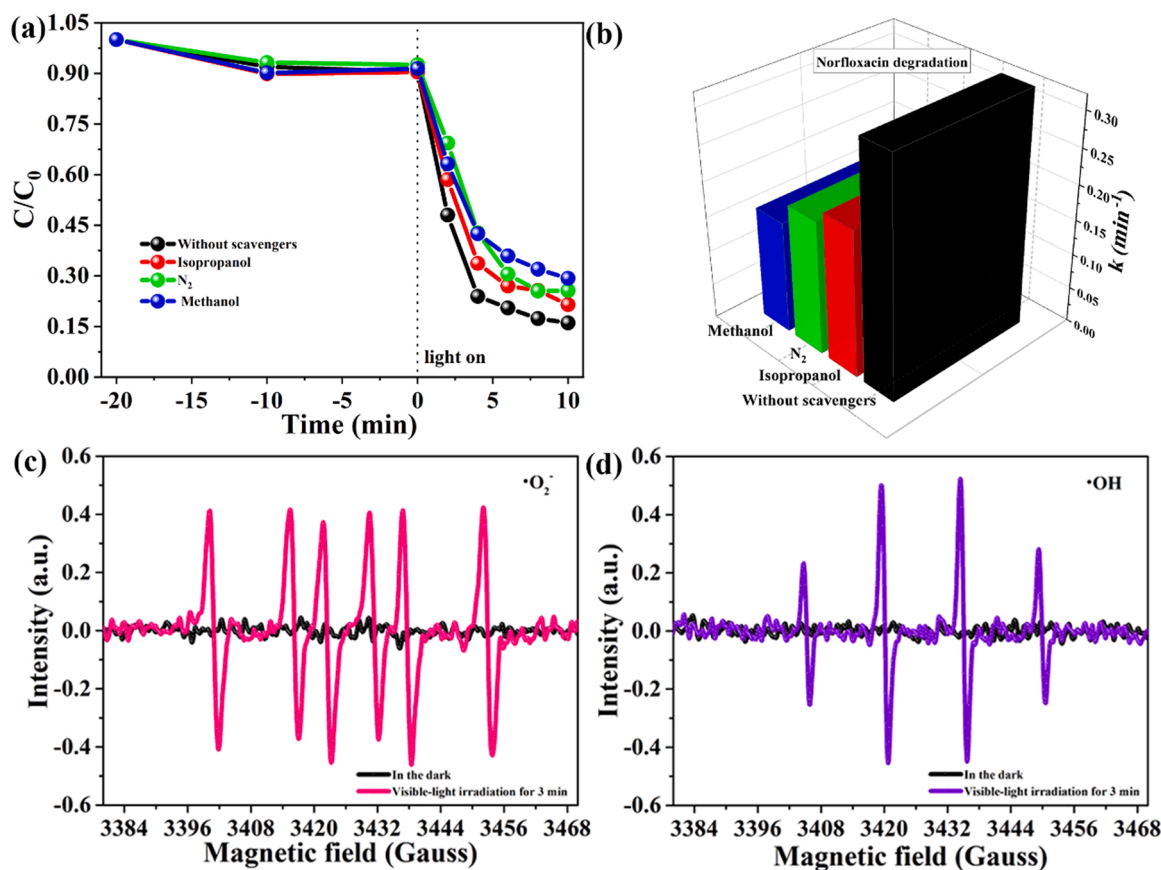


Fig. 6. (a, b) Trapping experiment of active species and corresponding first-order-kinetic plots with adding different scavengers; (c, d) DMPO spin-trapping ESR signals for DMPO- $\bullet\text{O}_2^-$  and DMPO- $\bullet\text{OH}$  over the  $\text{AgCl@Zr}^{3+}\text{-ZrO}_2$ -11 heterojunction.

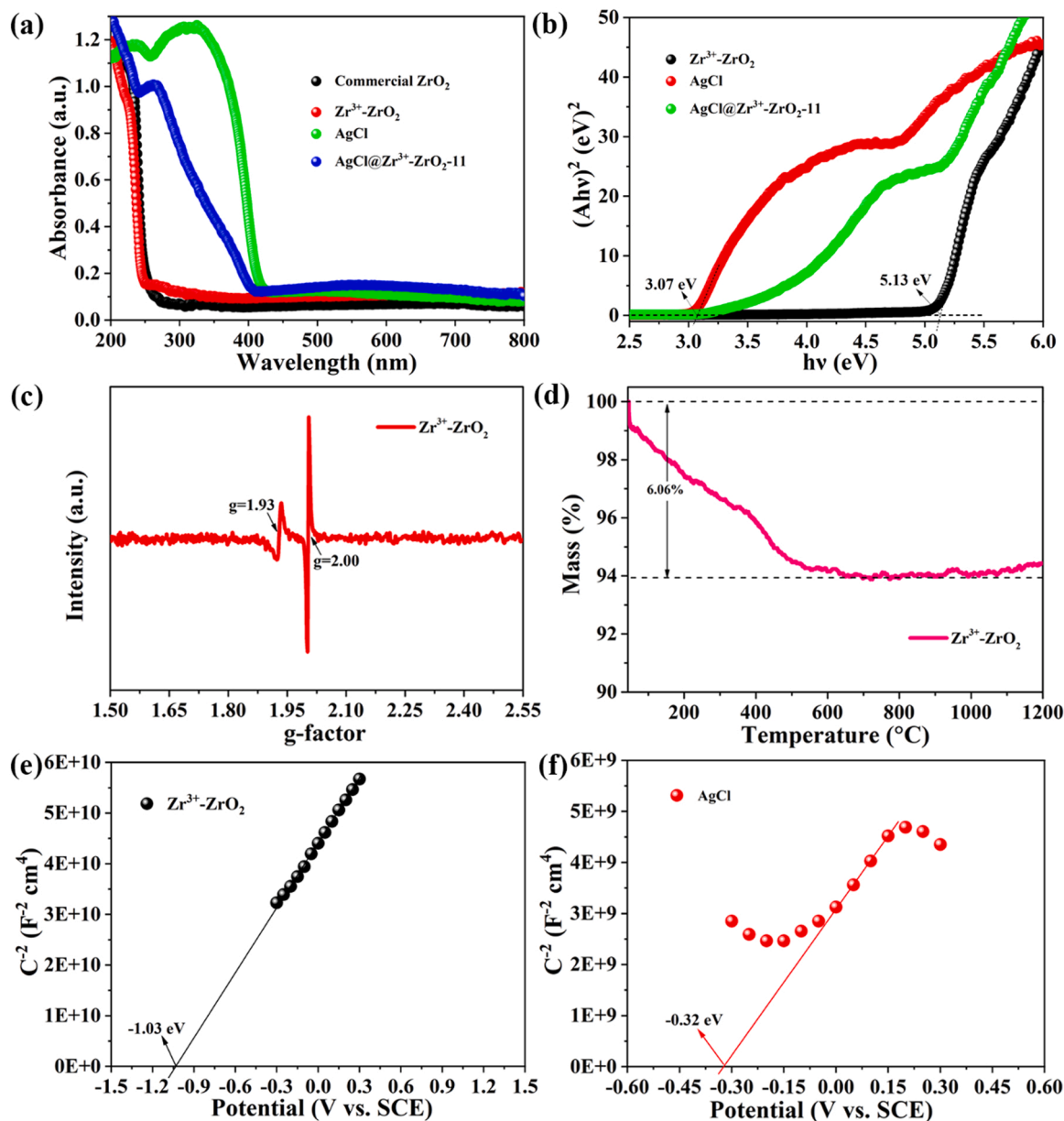


Fig. 7. (a, b) UV–visible diffuse reflectance absorption spectra and tauc plots of the samples; (c) Low temperature EPR spectra of  $\text{Zr}^{3+}$ - $\text{ZrO}_2$  clusters detected at 77 K; (d) TGA curves of  $\text{Zr}^{3+}$ - $\text{ZrO}_2$  clusters; (e, f) Mott-schottky plots of  $\text{Zr}^{3+}$ - $\text{ZrO}_2$  and AgCl.

demonstrating the formation of  $\text{Zr}^{3+}$  species. Besides, the following TGA curves for the prepared  $\text{Zr}^{3+}$ - $\text{ZrO}_2$  clusters also support the formation of the  $\text{Zr}^{3+}$  species. As shown in Fig. 7(d), we could observe a weak weight increase up to 900 °C, probably attributed to the oxidation of  $\text{Zr}^{3+}$  species into  $\text{Zr}^{4+}$  species, which is also consistent with the formation of  $\text{Zr}^{3+}$  species [11,45]. The surface carbon species over the  $\text{Zr}^{3+}$ - $\text{ZrO}_2$  clusters are determined to be approximately 6.06%, which is the consequence of the polymerization of small organic molecules during the modified solvothermal process. That is, the modified solvothermal reaction induces the formation of surface carbon materials as well as the generation of the  $\text{Zr}^{3+}$  species. In addition, the types and flat band potentials of the prepared AgCl and  $\text{Zr}^{3+}$ - $\text{ZrO}_2$  clusters were also studied by Mott-Schottky plots. As displayed in Fig. 7(e, f), the positive slopes of the plots for the prepared AgCl and  $\text{Zr}^{3+}$ - $\text{ZrO}_2$  clusters indicate the n-type semiconductors. The flat band potential values for the prepared AgCl and  $\text{Zr}^{3+}$ - $\text{ZrO}_2$  clusters are estimated to be  $-1.03$  and  $-0.32$  V (V vs. Saturated Calomel Electrode, SCE), approximately  $-0.79$  and  $+0.08$  V (vs NHE, Normal Hydrogen Electrode, pH = 0) according to

extrapolating the linear part of the Mott-Schottky plots, which are supposedly more positive to the conduction band with difference of 0–0.2 V [46,47]. Thus, the conduction band potential values of AgCl and  $\text{Zr}^{3+}$ - $\text{ZrO}_2$  clusters are determined to be  $-0.89$  and  $-0.18$  eV (vs NHE, pH = 0), respectively.

Based on the above results and analysis, possible visible-light photocatalytic mechanism for the prepared  $\text{AgCl@Zr}^{3+}$ - $\text{ZrO}_2$  heterojunctions towards norfloxacin degradation were proposed. At first, the ultraviolet photoelectron spectroscopy was measured to determine the discrepancy Fermi level ( $E_f$ ) for the  $\text{Zr}^{3+}$ - $\text{ZrO}_2$  clusters and AgCl [48]. As shown in Fig. 8(a), the work function ( $\Phi$ ) values of AgCl and  $\text{Zr}^{3+}$ - $\text{ZrO}_2$  clusters are determined to be approximately 6.03 and 2.87 eV, respectively, indicating a higher  $E_f$  of  $\text{Zr}^{3+}$ - $\text{ZrO}_2$  clusters compared with that of AgCl. Secondly, the detailed band structures of the prepared AgCl and  $\text{Zr}^{3+}$ - $\text{ZrO}_2$  clusters were also determined by the combinations of Mott-Schottky plots and tauc plots. As shown in Fig. 8(b), the valance band potentials values for the AgCl and  $\text{Zr}^{3+}$ - $\text{ZrO}_2$  clusters are determined to be  $+4.24$  and  $+2.16$  eV according to the formula of  $E_v = E_c$



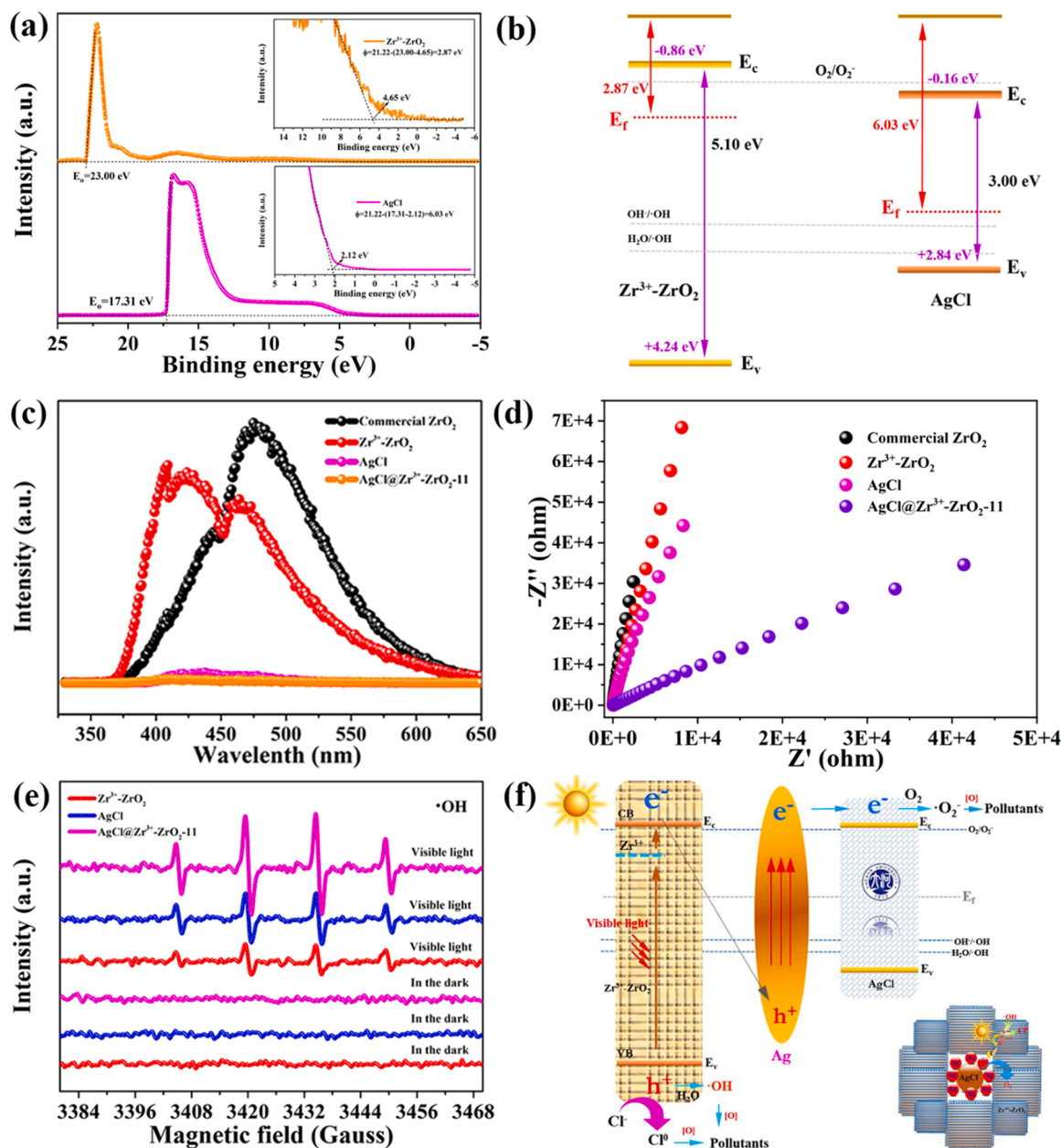


**Fig. 8.** (a) Ultraviolet photoelectron spectroscopy for AgCl and  $\text{Zr}^{3+}$ - $\text{ZrO}_2$  clusters; (b) Band structures for AgCl and  $\text{Zr}^{3+}$ - $\text{ZrO}_2$  clusters; (c, d) Fluorescence emission spectra and electrochemical impedance spectra for commercial  $\text{ZrO}_2$ , AgCl,  $\text{Zr}^{3+}$ - $\text{ZrO}_2$ , and AgCl@ $\text{Zr}^{3+}$ - $\text{ZrO}_2$ -11 heterojunction; (e) DMPO spin-trapping ESR signals for DMPO- $\bullet\text{OH}$  for AgCl,  $\text{Zr}^{3+}$ - $\text{ZrO}_2$ , and AgCl@ $\text{Zr}^{3+}$ - $\text{ZrO}_2$ -11 heterojunction; (f) Visible-light photocatalytic mechanism of AgCl@ $\text{Zr}^{3+}$ - $\text{ZrO}_2$  heterojunctions towards norfloxacin degradation (Insert indicates the schematic illustration of the locations for the generated  $\text{Ag}^0$  over AgCl and charge separation).

+  $E_g$  [11,49]. Apart from this, the electrochemical impedance spectra and fluorescence spectra of the samples also clearly revealed the remarkably enhanced charge separation and highly decreased interfacial migration resistance for the prepared AgCl@ $\text{Zr}^{3+}$ - $\text{ZrO}_2$  heterojunctions compared with those of pristine AgCl and  $\text{Zr}^{3+}$ - $\text{ZrO}_2$  clusters [50]. As shown in Fig. 8(c, d), the prepared AgCl@ $\text{Zr}^{3+}$ - $\text{ZrO}_2$  heterojunctions exhibit the smallest arc radius and weakest fluorescence emission signals compared with those of commercial  $\text{ZrO}_2$ ,  $\text{Zr}^{3+}$ - $\text{ZrO}_2$ , and AgCl, indicating the great advantages of the prepared AgCl@ $\text{Zr}^{3+}$ - $\text{ZrO}_2$  heterojunctions for efficient photocatalytic norfloxacin degradation. That is, the formed AgCl@ $\text{Zr}^{3+}$ - $\text{ZrO}_2$  heterojunctions would have a higher charge separation efficiency for enhanced photocatalysis. To further illuminate the visible-light photocatalytic mechanism of AgCl@ $\text{Zr}^{3+}$ - $\text{ZrO}_2$  heterojunctions, the DMPO- $\bullet\text{OH}$  EPR spectra for the prepared AgCl,  $\text{Zr}^{3+}$ - $\text{ZrO}_2$ , and AgCl@ $\text{Zr}^{3+}$ - $\text{ZrO}_2$ -11

heterojunction were detected under dark and visible-light illumination. As shown in Fig. 8(e), it can be found that pristine AgCl and  $\text{Zr}^{3+}$ - $\text{ZrO}_2$  clusters present no DMPO-radical  $\bullet\text{OH}$  signals in the dark and relatively weak DMPO-radical  $\bullet\text{OH}$  signals under visible-light illumination. To our surprise, the prepared AgCl@ $\text{Zr}^{3+}$ - $\text{ZrO}_2$ -11 heterojunction exhibits significantly improved DMPO-radical  $\bullet\text{OH}$  signals under visible-light illumination compared with those of the prepared AgCl and  $\text{Zr}^{3+}$ - $\text{ZrO}_2$  clusters, suggesting that the formation of AgCl@ $\text{Zr}^{3+}$ - $\text{ZrO}_2$  nanostructures contributes to the generation of more  $\bullet\text{OH}$  species [51]. That is, the strong combined interfaces between the AgCl and  $\text{Zr}^{3+}$ - $\text{ZrO}_2$  clusters are conducive to charge separation and formation of more  $\bullet\text{OH}$  species for high-efficiency photocatalytic norfloxacin degradation under visible-light illumination [52]. Fig. 8(f) shows the suggested photocatalytic mechanism for AgCl@ $\text{Zr}^{3+}$ - $\text{ZrO}_2$  heterojunctions towards norfloxacin degradation under visible-light illumination, the locations

of the generated  $\text{Ag}^0$  decomposed from  $\text{AgCl}$ , and photo-generated carriers' separation process. The obvious difference between commercial  $\text{ZrO}_2$  and the  $\text{Zr}^{3+}\text{-ZrO}_2$  clusters is the formation of  $\text{Zr}^{3+}$  species and rather high surface areas. Considering the core-shell structures of the  $\text{AgCl@Zr}^{3+}\text{-ZrO}_2$  heterojunctions, it could be concluded that  $\text{Ag}^0$  would be generated over the surface of  $\text{AgCl}$  and located between the  $\text{AgCl}$  and  $\text{Zr}^{3+}\text{-ZrO}_2$  clusters, as depicted in Fig. 8(f, insert), which would efficiently boost the charge separation. Under visible-light illumination, the  $\text{Zr}^{3+}\text{-ZrO}_2$  clusters would be excited and generate photo-generated electrons, while the  $\text{Ag}$  nanoparticles would also produce the photo-generated electrons and holes under visible-light illumination. Considering the much stronger oxidation ability of the photo-generated holes on the valance band of  $\text{Zr}^{3+}\text{-ZrO}_2$  clusters, trapping experiments, the work function ( $\Phi$ ) values of  $\text{AgCl}$ ,  $\text{Zr}^{3+}\text{-ZrO}_2$  clusters, and  $\text{Ag}^0$ , and the detection of DMPO spin-trapping ESR signals for  $\text{DMPO}\cdot\text{OH}$  over the  $\text{AgCl@Zr}^{3+}\text{-ZrO}_2$  nanostructures, a reasonable S-Scheme-like charge transfer pathways was suggested [11,41,53]. As shown in Fig. 8(f), the  $\text{Zr}^{3+}\text{-ZrO}_2$  clusters and  $\text{Ag}$  would generate photo-generated electrons and electrons under visible-light irradiation [22,54], and the photo-induced electrons of  $\text{Zr}^{3+}\text{-ZrO}_2$  clusters would migrate into the conduction band though  $\text{Zr}^{3+}$  defect level and would recombine with the photo-generated electrons of  $\text{Ag}$  for efficiently enhanced charge separation. Meanwhile, the photo-generated electrons in the excited  $\text{Ag}$  would transfer to  $\text{AgCl}$  for generation of  $\cdot\text{O}_2$  species for rapid photo-degradation of organic pollutants, and the holes in the valance band of  $\text{Zr}^{3+}\text{-ZrO}_2$  clusters, and the remaining holes on valance band of  $\text{Zr}^{3+}\text{-ZrO}_2$  clusters would be utilized for the oxidation of the  $\text{H}_2\text{O}$  and  $\text{Cl}^-$  species to produce  $\cdot\text{OH}$  species and  $\text{Cl}^0$  to decompose organic pollutants [19,55]. The self-doping could promote the visible-light excitation of  $\text{Zr}^{3+}\text{-ZrO}_2$  clusters and form S-scheme like long-distance charge transfer pathways between  $\text{Zr}^{3+}\text{-ZrO}_2$  clusters and  $\text{AgCl}$ , resulting in remarkably enhanced visible-light photocatalytic performance and strong redox

capacity of the  $\text{AgCl@Zr}^{3+}\text{-ZrO}_2$  heterojunctions.

### 3.5. Visible-light photocatalytic degradation pathways

To well understanding the detailed visible-light photocatalytic norfloxacin degradation process, LC-MS were performed to detect the intermediate products of the degraded norfloxacin over the  $\text{AgCl@Zr}^{3+}\text{-ZrO}_2$  heterojunctions under visible-light illumination. Fig. S7 shows the LC-MS of the degraded norfloxacin solution over the  $\text{AgCl@Zr}^{3+}\text{-ZrO}_2$  heterojunction at 0, 2, 6, and 10 min. As exhibited in Figs. S7(a, b), pristine norfloxacin solution and the norfloxacin solution at 0 min present only one strong LC-MS signal at  $m/z = 320$ , which corresponds to norfloxacin molecules, while the degraded norfloxacin solution under visible-light illumination shows many different LC-MS signals at  $m/z = 404, 362, 322, 320, 302, 274, 246$ , and 152, as displayed in Figs. S7(c-e). These findings confirm the visible-light photodecomposition of norfloxacin molecules and the generation of many different intermediate products under visible-light illumination. Based on the LC-MS results, reasonable photocatalytic norfloxacin degradation pathways over the  $\text{AgCl@Zr}^{3+}\text{-ZrO}_2$  heterojunctions under visible-light illumination were suggested, as shown in Fig. 9(a). Under visible-light irradiation, the norfloxacin molecules would firstly generate the intermediate products of P1 ( $m/z = 322$ ), P4 ( $m/z = 302$ ), P7 ( $m/z = 362$ ), and P8 ( $m/z = 404$ ) via reduction, ring-opening, oxidation, displacement, and losing fluorine reactions [40,56,57]. In addition, the P1 ( $m/z = 322$ ) would be probably decomposed into the intermediate products of P2 ( $m/z = 294$ ) and P3 ( $m/z = 246$ ) via decarboxylation, demethylation, and displacement reactions [40,57], and finally transform into the intermediate product of P6 ( $m/z = 152$ ). Meanwhile, P4 ( $m/z = 302$ ) would lose methyl group to generate the intermediate product of P5 ( $m/z = 274$ ) and finally to generate the intermediate product of P6 ( $m/z = 152$ ) [56–58].

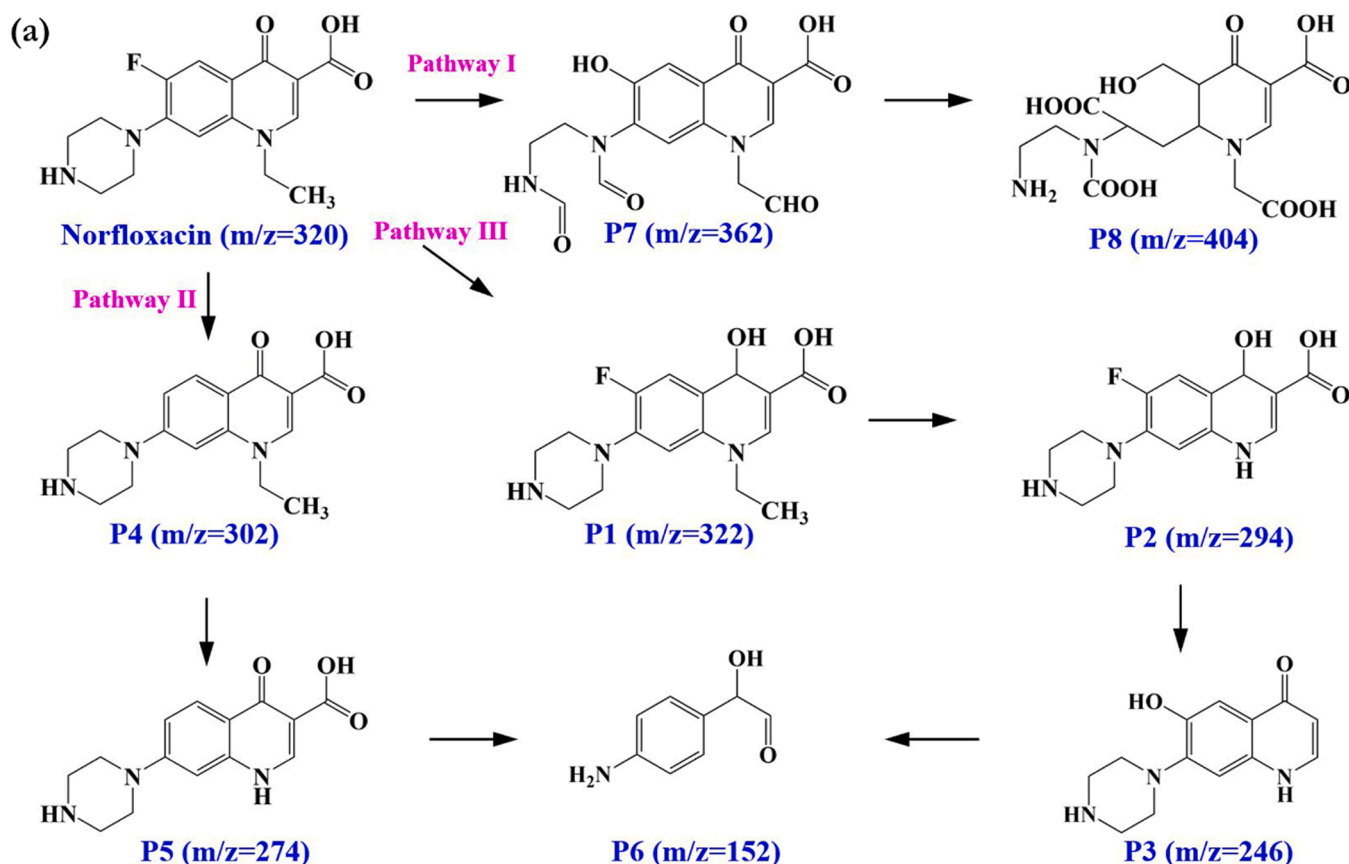


Fig. 9. Suggested norfloxacin degradation pathways over  $\text{AgCl@Zr}^{3+}\text{-ZrO}_2$  heterojunctions under visible-light illumination.

## 4. Conclusions

In summary, self-doped  $\text{Zr}^{3+}$ - $\text{ZrO}_2$  clusters with high BET surface area and nanostructured  $\text{AgCl@Zr}^{3+}$ - $\text{ZrO}_2$  heterojunctions have been fabricated for remarkably enhanced photodegradation of emerging organic pollutants, including norfloxacin, bisphenol A, 4-Nitro-m-cresol, carbamazepine, and tetracycline. The experimental results show that the absorbed surface chlorine over  $\text{Zr}^{3+}$ - $\text{ZrO}_2$  clusters induces the oriented adhesions of  $\text{Ag}^+$  to form  $\text{AgCl@Zr}^{3+}$ - $\text{ZrO}_2$  nanostructures with strongly combined interfaces. More importantly, the prepared  $\text{AgCl@Zr}^{3+}$ - $\text{ZrO}_2$  heterojunctions present remarkably enhanced charge separation and ultra-high photocatalytic performance towards norfloxacin degradation under visible-light illumination. The prepared nanostructured  $\text{AgCl@Zr}^{3+}$ - $\text{ZrO}_2$ -11 heterojunction exhibits the maximum rate constants of approximately  $0.21989 \text{ min}^{-1}$ , which is 62.12 times of the  $\text{Zr}^{3+}$ - $\text{ZrO}_2$  clusters and 21.95 times of  $\text{AgCl}$ , mainly attributed to the formation of self-doped  $\text{Zr}^{3+}$ - $\text{ZrO}_2$  clusters, strongly established interfaces between  $\text{AgCl}$  and  $\text{Zr}^{3+}$ - $\text{ZrO}_2$  nanoclusters, and rather high specific surface areas. In addition, we also observe an increased TOC removal rates of norfloxacin enabled by  $\text{AgCl@Zr}^{3+}$ - $\text{ZrO}_2$  heterojunctions under visible-light illumination. Current work indicates a high-performance and stabilized unique nanostructured heterojunctions for dealing with emerging organic pollutants.

## CRediT authorship contribution statement

**Xin Yu:** Conceptualization, Writing – review & editing. **Chao Zhou:** Methodology, Investigation, Writing – original draft. **Zhanhua Huang:** Formal analysis, Writing – review & editing. **Changhui Xin:** Investigation, Data curation, Resources. **Yanjing Lin:** Validation, Software. **Fengdan Fu:** Formal analysis, Visualization. **Shijie Li:** Software, Writing – review & editing. **Weiping Zhang:** Supervision, Writing – review & editing.

## Declaration of Competing Interest

The authors declare that they have no known competing financial interests or personal relationships that could have appeared to influence the work reported in this paper.

## Data availability

Data will be made available on request.

## Acknowledgements

This work was financially supported by the Scientific and Technological Project of Henan Province (No. 202102310607), China Postdoctoral Science Foundation (No. 2019M652526), Scientific Research Project for Higher Education of Henan Province (22A610008), Postgraduate Cultivating Innovation and Quality Improvement Action Plan of Henan University (CX3040A0970124), and College Students' Innovative Entrepreneurial Training Plan Program of Henan University (20221015019).

## Appendix A. Supporting information

Supplementary data associated with this article can be found in the online version at [doi:10.1016/j.apcatb.2022.122308](https://doi.org/10.1016/j.apcatb.2022.122308).

## References

- [1] E.A. Noman, A. Al-Gheethi, R.M.S.R. Mohamed, B.A. Talip, M.S. Hossain, W.A. H. Altowayti, N. Ismail, Sustainable approaches for removal of cephalixin antibiotic from non-clinical environments: a critical review, *J. Hazard. Mater.* 417 (2021), 126040.
- [2] Y. Gao, Y. Ji, G. Li, T. An, Mechanism, kinetics and toxicity assessment of OH-initiated transformation of triclosan in aquatic environments, *Water Res.* 49 (2014) 360–370.
- [3] Y. Gao, Y. Ji, G. Li, T. An, Theoretical investigation on the kinetics and mechanisms of hydroxyl radical-induced transformation of parabens and its consequences for toxicity: influence of alkyl-chain length, *Water Res.* 91 (2016) 77–85.
- [4] J.H. Carey, J. Lawrence, H.M. Tosine, Photodechlorination of PCB's in the presence of titanium dioxide in aqueous suspensions, *Bull. Environ. Contam. Toxicol.* 16 (1976) 697–701.
- [5] S. Li, M. Cai, Y. Liu, C. Wang, R. Yan, X. Chen, Constructing  $\text{Cd}_{0.5}\text{Zn}_{0.5}\text{S}/\text{Bi}_2\text{WO}_6$  S-scheme heterojunction for boosted photocatalytic antibiotic oxidation and  $\text{Cr(VI)}$  reduction, *Adv. Powder Mater.* 2 (2023), 100073.
- [6] H. Wang, L. Zhang, Z. Chen, J. Hu, S. Li, Z. Wang, J. Liu, X. Wang, Semiconductor heterojunction photocatalysts: design, construction, and photocatalytic performances, *Chem. Soc. Rev.* 43 (2014) 5234–5244.
- [7] T. Hisatomi, J. Kubota, K. Domen, Recent advances in semiconductors for photocatalytic and photoelectrochemical water splitting, *Chem. Soc. Rev.* 43 (2014) 7520–7535.
- [8] T. Do Minh, J. Song, A. Deb, L. Cha, V. Srivastava, M. Sillanpää, Biochar based catalysts for the abatement of emerging pollutants: a review, *Chem. Eng. J.* 394 (2020), 124856.
- [9] Y. Guo, C. Xin, L. Dai, Y. Zhang, X. Yu, Q. Guo, Layered and porous (Al,C)- $\text{Ta}_2\text{O}_5$  mesocrystals supported CdS quantum dots for high-efficiency photodegradation of organic contaminants, *Sep. Purif. Technol.* 284 (2022), 120297.
- [10] J. Yu, Y. Guo, Y. Zhao, M. Hou, X. Yu, S. Li, Visible-light photocatalytic tetracycline degradation over nanodots-assembled  $\text{N-ZrO}_2$ -x nanostructures: performance, degradation pathways and mechanistic insight, *J. Alloy. Compd.* 895 (2022), 162582.
- [11] J. Huang, J. Liu, L. Tian, X. Li, X. Ma, X. Yu, Q. Guo, J. Zhao, Ultrathin carbon-coated  $\text{Zr}^{3+}$ - $\text{ZrO}_2$  nanostructures for efficient visible light photocatalytic antibiotic elimination, *Chem. Eng. J.* 412 (2021), 128621.
- [12] A. Punnoose, M.S. Seehra, ESR observation of  $\text{W}^{5+}$  and  $\text{Zr}^{3+}$  states in  $\text{Pt}/\text{WO}_3/\text{ZrO}_2$  catalysts, *Catal. Lett.* 78 (2002) 157–160.
- [13] C.V. Reddy, I.N. Reddy, K. Ravindranadh, K.R. Reddy, N.P. Shetti, D. Kim, J. Shim, T.M. Aminabhavi, Copper-doped  $\text{ZrO}_2$  nanoparticles as high-performance catalysts for efficient removal of toxic organic pollutants and stable solar water oxidation, *J. Environ. Manag.* 260 (2020), 110088.
- [14] C.F. Carbuloni, J.E. Savoia, J.S.P. Santos, C.A.A. Pereira, R.G. Marques, V.A. S. Ribeiro, A.M. Ferrari, Degradation of metformin in water by  $\text{TiO}_2$ - $\text{ZrO}_2$  photocatalysis, *J. Environ. Manag.* 262 (2020), 110347.
- [15] H. Anwer, J.-W. Park, Synthesis and characterization of a heterojunction  $\text{rGO}/\text{ZrO}_2/\text{Ag}_3\text{PO}_4$  nanocomposite for degradation of organic contaminants, *J. Hazard. Mater.* 358 (2018) 416–426.
- [16] Q. Wang, K. Edalati, Y. Koganemaru, S. Nakamura, M. Watanabe, T. Ishihara, Z. Horita, Photocatalytic hydrogen generation on low-bandgap black zirconia ( $\text{ZrO}_2$ ) produced by high-pressure torsion, *J. Mater. Chem. A* 8 (2020) 3643–3650.
- [17] J. Wang, J. Huang, J. Meng, Q. Li, J. Yang, Double-hole codoped huge-gap semiconductor  $\text{ZrO}_2$  for visible-light photocatalysis, *Phys. Chem. Chem. Phys.* 18 (2016) 17517–17524.
- [18] X. Yu, J.L. Huang, J.J. Zhao, S.F. Liu, D.D. Xiang, Y.T. Tang, J. Li, Q.H. Guo, X. Q. Ma, J.W. Zhao, Efficient visible light photocatalytic antibiotic elimination performance induced by nanostructured  $\text{Ag}/\text{AgCl}/\text{Ti}^{3+}$ - $\text{TiO}_2$  mesocrystals, *Chem. Eng. J.* 403 (2021), 128621.
- [19] X.-J. Wen, C.-G. Niu, D.-W. Huang, L. Zhang, C. Liang, G.-M. Zeng, Study of the photocatalytic degradation pathway of norfloxacin and mineralization activity using a novel ternary  $\text{Ag}/\text{AgCl}-\text{CeO}_2$  photocatalyst, *J. Catal.* 355 (2017) 73–86.
- [20] H. Sudrajat, S. Babel, H. Sakai, S. Takizawa, Rapid enhanced photocatalytic degradation of dyes using novel N-doped  $\text{ZrO}_2$ , *J. Environ. Manag.* 165 (2016) 224–234.
- [21] M. Kruk, M. Jaroniec, Gas Adsorption Characterization of ordered organic–inorganic nanocomposite materials, *Chem. Mater.* 13 (2001) 3169–3183.
- [22] R. Qiao, M. Mao, E. Hu, Y. Zhong, J. Ning, Y. Hu, Facile formation of mesoporous  $\text{BiVO}_4/\text{Ag}/\text{AgCl}$  heterostructured microspheres with enhanced visible-light photoactivity, *Inorg. Chem.* 54 (2015) 9033–9039.
- [23] G. Zhou, L. Shen, Z. Xing, X. Kou, S. Duan, L. Fan, H. Meng, Q. Xu, X. Zhang, L. Li, M. Zhao, J. Mi, Z. Li,  $\text{Ti}^{3+}$  self-doped mesoporous black  $\text{TiO}_2$ /graphene assemblies for unpredicted-high solar-driven photocatalytic hydrogen evolution, *J. Colloid Interface Sci.* 505 (2017) 1031–1038.
- [24] X. Shi, M. Fujitsuka, Z. Lou, P. Zhang, T. Majima, In situ nitrogen-doped hollow- $\text{TiO}_2$ /g- $\text{C}_3\text{N}_4$  composite photocatalysts with efficient charge separation boosting water reduction under visible light, *J. Mater. Chem. A* 5 (2017) 9671–9681.
- [25] J. Tang, Y. Liu, Y. Hu, G. Lv, C. Yang Guangcheng, Carbothermal reduction induced  $\text{Ti}^{3+}$  self-doped  $\text{TiO}_2$ /GQD nanohybrids for high-performance visible light photocatalysis, *Chem. Eur. J.* 24 (2018) 4390–4398.
- [26] C. Xin, S. Zhu, J. Liao, M. Hou, Q. Li, X. Yu, S. Li, Rational design of S-scheme  $\text{AgI}/\text{ZrTiO}_{4-x}$  heterojunctions for remarkably boosted norfloxacin degradation, *Chemosphere* 308 (2022), 136279.
- [27] W.-S. Liu, M.-W. Liao, S.-H. Huang, Y.I.A. Reyes, H.-Y. Tiffany Chen, T.-P. Perng, Formation and characterization of gray  $\text{Ta}_2\text{O}_5$  and its enhanced photocatalytic hydrogen generation activity, *Int. J. Hydrog. Energy* 45 (2020) 16560–16568.
- [28] C. Li, S. Yu, X. Zhang, Y. Wang, C. Liu, G. Chen, H. Dong, Insight into photocatalytic activity, universality and mechanism of copper/chlorine surface dual-doped graphitic carbon nitride for degrading various organic pollutants in water, *J. Colloid Interface Sci.* 538 (2019) 462–473.



- [29] X. Yu, J.J. Zhao, J.L. Huang, J.W. Zhao, Y.F. Guo, Y.T. Tang, X.Q. Ma, Z.H. Li, Q. H. Guo, J.W. Zhao, Visible light photocatalysis of amorphous  $\text{Cl-Ta}_2\text{O}_5-x$  microspheres for stabilized hydrogen generation, *J. Colloid Interface Sci.* 572 (2020) 141–150.
- [30] R. Ning, H. Pang, Z. Yan, Z. Lu, Q. Wang, Z. Wu, W. Dai, L. Liu, Z. Li, G. Fan, X. Fu, An innovative S-scheme  $\text{AgCl}/\text{MIL-100}(\text{Fe})$  heterojunction for visible-light-driven degradation of sulfamethazine and mechanism insight, *J. Hazard. Mater.* 435 (2022), 129061.
- [31] J. Huang, S. Liu, W. Long, Q. Wang, X. Yu, S. Li, Highly enhanced photodegradation of emerging pollutants by  $\text{Ag}/\text{AgCl}/\text{Ta}_2\text{O}_5-x$  mesocrystals, *Sep. Purif. Technol.* 279 (2021), 119733.
- [32] J. Wu, X. Fang, H. Dong, L. Lian, N. Ma, W. Dai, Bimetallic silver/bismuth-MOFs derived strategy for  $\text{Ag}/\text{AgCl}/\text{BiOCl}$  composite with extraordinary visible light-driven photocatalytic activity towards tetracycline, *J. Alloy. Compd.* 877 (2021), 160262.
- [33] F. Mu, C. Liu, Y. Xie, S. Zhou, B. Dai, D. Xia, H. Huang, W. Zhao, C. Sun, Y. Kong, D. Y.C. Leung, Metal-organic framework-derived rodlike  $\text{AgCl}/\text{Ag}/\text{In}_2\text{O}_3$ : a plasmonic Z-scheme visible light photocatalyst, *Chem. Eng. J.* 415 (2021), 129010.
- [34] H. Lv, Y. Duan, X. Zhou, G. Liu, X. Wang, Y. Wang, M. Yuan, Q. Meng, C. Wang, Visible-light-driven  $\text{Ag}/\text{AgCl}/\text{In}_2\text{O}_3$ : a ternary photocatalyst for the degradation of tetracycline antibiotics, *Catal. Sci. Technol.* 10 (2020) 8230–8239.
- [35] Q. Chen, W. Yang, J. Zhu, L. Fu, D. Li, L. Zhou, Enhanced visible light photocatalytic activity of  $\text{g-C}_3\text{N}_4$  decorated  $\text{ZrO}_2-x$  nanotubes heterostructure for degradation of tetracycline hydrochloride, *J. Hazard. Mater.* 384 (2020), 121275.
- [36] C. Wang, M. Cai, Y. Liu, F. Yang, H. Zhang, J. Liu, S. Li, Facile construction of novel organic-inorganic tetra (4-carboxyphenyl) porphyrin/ $\text{Bi}_2\text{MoO}_6$  heterojunction for tetracycline degradation: performance, degradation pathways, intermediate toxicity analysis and mechanism insight, *J. Colloid Interface Sci.* 605 (2022) 727–740.
- [37] T. An, H. Yang, G. Li, W. Song, W.J. Cooper, X. Nie, Kinetics and mechanism of advanced oxidation processes (AOPs) in degradation of ciprofloxacin in water, *Appl. Catal. B Environ.* 94 (2010) 288–294.
- [38] W. Wang, H. Wang, G. Li, P.K. Wong, T. An, Visible light activation of persulfate by magnetic hydrochar for bacterial inactivation: efficiency, recyclability and mechanisms, *Water Res.* 176 (2020), 115746.
- [39] H. Fang, Y. Gao, G. Li, J. An, P.-K. Wong, H. Fu, S. Yao, X. Nie, T. An, Advanced oxidation kinetics and mechanism of preservative propylparaben degradation in aqueous suspension of  $\text{TiO}_2$  and risk assessment of its degradation products, *Environ. Sci. Technol.* 47 (2013) 2704–2712.
- [40] Z. Wu, J. Yu, W. Wang, C. Xin, X. Yu, Y. Tang, High-performance photodegradation of norfloxacin enabled by  $\text{AgI}/\text{Ag}_3\text{PO}_4$  nanostructures, *J. Alloy. Compd.* 891 (2022), 161877.
- [41] J. Liu, M. Ma, X. Yu, C. Xin, M. Li, S. Li, Constructing Ag decorated  $\text{ZnS}_{1-x}$  quantum dots/ $\text{Ta}_2\text{O}_5-x$  nanospheres for boosted tetracycline removal: synergetic effects of structural defects, S-scheme heterojunction, and plasmonic effects, *J. Colloid Interface Sci.* 623 (2022) 1085–1100.
- [42] R. Dong, B. Tian, C. Zeng, T. Li, T. Wang, J. Zhang, Ecofriendly synthesis and photocatalytic activity of uniform cubic  $\text{Ag}/\text{AgCl}$  plasmonic photocatalyst, *J. Phys. Chem. C* 117 (2013) 213–220.
- [43] W. Li, L.B. Feng, Y.Q. Yin, Correlation between the catalytic property and  $\text{Zr}^{3+}$  ion for  $\text{ZrO}_2$  in CO hydrogenation, *Chin. Chem. Lett.* 7 (1996) 269–270.
- [44] J. Li, M. Zhang, Z. Guan, Q. Li, C. He, J. Yang, Synergistic effect of surface and bulk single-electron-trapped oxygen vacancy of  $\text{TiO}_2$  in the photocatalytic reduction of  $\text{CO}_2$ , *Appl. Catal. B Environ.* 206 (2017) 300–307.
- [45] B. Jiang, Y. Tang, Y. Qu, J.-Q. Wang, Y. Xie, C. Tian, W. Zhou, H. Fu, Thin carbon layer coated  $\text{Ti}^{3+}$ - $\text{TiO}_2$  nanocrystallites for visible-light driven photocatalysis, *Nanoscale* 7 (2015) 5035–5045.
- [46] S. Adhikari, S. Mandal, D.-H. Kim, 1D/2D constructed  $\text{Bi}_2\text{S}_3/\text{Bi}_2\text{O}_2\text{CO}_3$  direct Z-scheme heterojunction: a versatile photocatalytic material for boosted photodegradation, photoreduction and photoelectrochemical detection of water-based contaminants, *J. Hazard. Mater.* 418 (2021), 126263.
- [47] S. Zhou, M. Hou, Y. Sun, W. Zhao, H. Wang, Q. Guo, X. Yu, X. Ma, J. Zhao, Ultrahigh-performance visible-light photodegradation enabled by direct Z-scheme  $\text{AgI}/(\text{Na},\text{F})-\text{C}_3\text{N}_4$  composites, *Compos. Part B Eng.* 224 (2021), 109200.
- [48] S. Feng, M. Yu, T. Xie, T. Li, D. Kong, J. Yang, C. Cheng, H. Chen, J. Wang,  $\text{MoS}_2/\text{CoFe}_2\text{O}_4$  heterojunction for boosting photogenerated carrier separation and the dominant role in enhancing peroxymonosulfate activation, *Chem. Eng. J.* 433 (2022), 134467.
- [49] X. Yu, J. Huang, J. Zhao, C. Zhou, C. Xin, Q. Guo, Topotactic formation of poriferous (Al,C)- $\text{Ta}_2\text{O}_5$  mesocrystals for improved visible-light photocatalysis, *J. Environ. Manag.* 304 (2022), 114289.
- [50] X. Li, S. Song, Y. Gao, L. Ge, W. Song, T. Ma, J. Liu, Identification of the charge transfer channel in cobalt encapsulated hollow nitrogen-doped carbon matrix@ $\text{CdS}$  heterostructure for photocatalytic hydrogen evolution, *Small* 17 (2021), 210131.
- [51] Q. Xu, L. Zhang, B. Cheng, J. Fan, J. Yu, S-scheme heterojunction photocatalyst, *Chem* 6 (2020) 1543–1559.
- [52] C. Wang, S. Li, M. Cai, R. Yan, K. Dong, J. Zhang, Y. Liu, Rationally designed tetra (4-carboxyphenyl) porphyrin/graphene quantum dots/bismuth molybdate Z-scheme heterojunction for tetracycline degradation and  $\text{Cr}(\text{VI})$  reduction: performance, mechanism, intermediate toxicity appraisalment, *J. Colloid Interface Sci.* 619 (2022) 307–321.
- [53] Y. Gong, X. Zhao, H. Zhang, B. Yang, K. Xiao, T. Guo, J. Zhang, H. Shao, Y. Wang, G. Yu, MOF-derived nitrogen doped carbon modified  $\text{g-C}_3\text{N}_4$  heterostructure composite with enhanced photocatalytic activity for bisphenol A degradation with peroxymonosulfate under visible light irradiation, *Appl. Catal. B Environ.* 233 (2018) 35–45.
- [54] X. Yao, X. Liu, One-pot synthesis of ternary  $\text{Ag}_2\text{CO}_3/\text{Ag}/\text{AgCl}$  photocatalyst in natural geothermal water with enhanced photocatalytic activity under visible light irradiation, *J. Hazard. Mater.* 280 (2014) 260–268.
- [55] Y. Zhu, R. Zhu, Y. Xi, T. Xu, L. Yan, J. Zhu, G. Zhu, H. He, Heterogeneous photo-Fenton degradation of bisphenol A over  $\text{Ag}/\text{AgCl}/\text{ferrihydrite}$  catalysts under visible light, *Chem. Eng. J.* 346 (2018) 567–577.
- [56] G. Li, S. Huang, N. Zhu, H. Yuan, D. Ge, Near-infrared responsive upconversion glass-ceramic/ $\text{BiOBr}$  heterojunction for enhanced photodegradation performances of norfloxacin, *J. Hazard. Mater.* 403 (2021), 123981.
- [57] N.S. Shah, J.A. Khan, M. Sayed, Z.U.H. Khan, A.D. Rizwan, N. Muhammad, G. Boczkaj, B. Murtaza, M. Imran, H.M. Khan, G. Zaman, Solar light driven degradation of norfloxacin using as-synthesized  $\text{Bi}^{3+}$  and  $\text{Fe}^{2+}$  co-doped  $\text{ZnO}$  with the addition of  $\text{HSO}_5^-$ : toxicities and degradation pathways investigation, *Chem. Eng. J.* 351 (2018) 841–855.
- [58] R. Su, L. Huang, N. Li, L. Li, B. Jin, W. Zhou, B. Gao, Q. Yue, Q. Li, Chlorine dioxide radicals triggered by chlorite under visible-light irradiation for enhanced degradation and detoxification of norfloxacin antibiotic: radical mechanism and toxicity evaluation, *Chem. Eng. J.* 414 (2021), 128768.